Accepted Manuscript

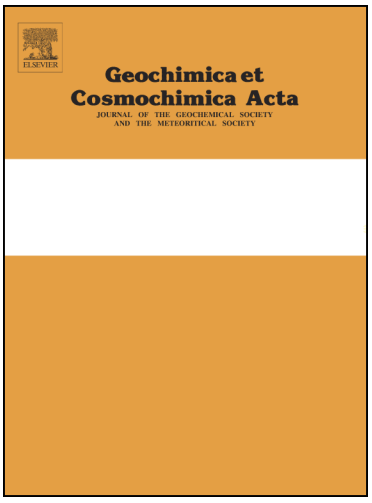

Toward an Understanding of Surface Layer Formation, Growth, and Transformation at the Glass–Fluid Interface

J. Hopf, J.R. Eskelsen, M. Chiu, A.V. Ievlev, O.S. Ovchinnikova, D. Leonard, E.M. Pierce

PII: S0016-7037(18)30065-6
DOI: https://doi.org/10.1016/j.gca.2018.01.035
Reference: GCA 10638

To appear in: *Geochimica et Cosmochimica Acta*

Received Date: 12 March 2017
Accepted Date: 30 January 2018

Please cite this article as: Hopf, J., Eskelsen, J.R., Chiu, M., Ievlev, A.V., Ovchinnikova, O.S., Leonard, D., Pierce, E.M., Toward an Understanding of Surface Layer Formation, Growth, and Transformation at the Glass–Fluid Interface, *Geochimica et Cosmochimica Acta* (2018), doi: https://doi.org/10.1016/j.gca.2018.01.035

This is a PDF file of an unedited manuscript that has been accepted for publication. As a service to our customers we are providing this early version of the manuscript. The manuscript will undergo copyediting, typesetting, and review of the resulting proof before it is published in its final form. Please note that during the production process errors may be discovered which could affect the content, and all legal disclaimers that apply to the journal pertain.

ACCEPTED MANUSCRIPT

TOWARD AN UNDERSTANDING OF SURFACE LAYER FORMATION, GROWTH, AND TRANSFORMATION AT THE GLASS-FLUID INTERFACE

Authors: J Hopf[1‡], JR Eskelsen[1‡], M Chiu[1], AV Ievlev[2], OS Ovchinnikova[2], D Leonard[3], and EM Pierce[1*]

Affiliations:

[1]Environmental Sciences Division, Oak Ridge National Laboratory (USA);

[2]Center for Nanophase Material Sciences, Oak Ridge National Laboratory (USA);

[3]Material Science and Technology, Oak Ridge National Laboratory (USA);

*Corresponding Author: Email: pierceem@ornl.gov, Phone: (865) 574-9968

[‡]J Hopf and J Eskelsen contributed equally to this work and are represented here as co-first authors.

Key Words: Quantitative Nanomechanical Peak Force® TappingMode™; atomic force microscopy; borosilicate glass corrosion; leaching mechanism; interfacial dissolution reprecipitation; silica diagenesis; altered layer; scanning transmission electron microscopy electron energy loss spectroscopy spectrum imaging

This manuscript has been authored by UT-Battelle, LLC under Contract No. DE-AC05-00OR22725 with the U.S. Department of Energy. The United States Government retains and the publisher, by accepting the article for publication, acknowledges that the United States Government retains a non-exclusive, paid-up, irrevocable, worldwide license to publish or reproduce the published form of this manuscript, or allow others to do so, for United States Government purposes. The Department of Energy will provide public access to these results of federally sponsored research in accordance with the DOE Public Access Plan (http://energy.gov/downloads/doe-publicaccess-plan).

ACCEPTED MANUSCRIPT

ACCEPTED MANUSCRIPT

ABSTRACT:

Silicate glass is a metastable and durable solid that has application to a number of energy and environmental challenges (e.g., microelectronics, fiber optics, and nuclear waste storage). If allowed to react with water over time silicate glass develops an altered layer at the solid-fluid interface. In this study, we used borosilicate glass (LAWB45) as model material to develop a robust understanding of altered layer formation (i.e., amorphous hydrated surface layer and crystalline reaction products). Experiments were conducted at high surface area-to-volume ratio (~200,000 m^{-1}) and 90 °C in the pressurized unsaturated flow (PUF) apparatus for 1.5-years to facilitate the formation of thick altered layers and allow for the effluent solution chemistry to be monitored continuously. A variety of microscopy techniques were used to characterized reacted grains and suggest the average altered layer thickness is 13.2 ±8.3 μm with the hydrated and clay layer representing 74.8% and 25.2% of the total altered layer, respectively. This estimate is within the experimental error of the value estimated from the B release rate data (~10 ±1 μm/yr) over the 1.5-year duration. PeakForce® quantitative nanomechanical mapping results suggest the hydrated layer has a modulus that ranges between ~20 to 40 GPa, which is in the range of porous silica that contains from ~20 to ~50% porosity, yet significantly lower than dense silica (~70 to 80 GPa). Scanning transmission electron microscopy (STEM) images confirm the presence of pores and an analysis of a higher resolution image of a region provides a qualitative estimate of ≥ 22% porosity in this layer with variations in the hydrated layer in void volume with increasing distance from the unaltered glass. Chemical composition analyses, based on a combination of time-of-flight secondary-ion mass spectrometry (ToF-SIMS) and scanning electron microscopy with X-ray energy dispersive spectroscopy (EDS) and STEM-EDS, clearly show that the altered layer is mainly composed of Al, H, Si, and O with the clay layer being enriched in Li, Zn, Fe, and Mg. The amorphous hydrated layer is enriched in Ca, H, and Zr with a minor amount of K. Furthermore, ToF-SIMS results also suggest the B profile is anti-correlated with the H profile in the hydrated layer. Our selected-area electron diffraction results suggest the structure of the hydrated layer closely resembles opal-AG (amorphous gel-like) with an average

ACCEPTED MANUSCRIPT

crystallite size of ~0.7 nm which is smaller than the critical nucleus for silica nanoparticles (i.e., 1.4 to 3 nm). These results suggest the hydrated layer is more consistent with a polymeric gel rather than a colloidal gel and is comprised of molecular units (<1 nm in size) that result from the difficult to hydrolyze bonds, such as Si—O—Zr units, during the glass corrosion process. The size of individual particles or molecular units is a function of formation conditions (e.g., pH, ionic strength, nano-confinement, solute composition) in the hydrated layer.

ACCEPTED MANUSCRIPT

ACCEPTED MANUSCRIPT

1 INTRODUCTION

Silicate glass is a metastable and durable solid that has application to a number of health, energy and environmental challenges (e.g., tissue engineering, microelectronics, fiber optics, and nuclear waste storage) (Gin et al., 2013; Smith et al., 2009; Stone-Weiss et al., 2018). Although multicomponent glass is sufficiently resistant to weathering for the service life of most industrial applications, if allowed to react with water over geologic time scales, a layer of reaction products forms on the surface of this metastable solid. The type of reaction products and rate of formation depends on the glass composition and environmental conditions (e.g., temperature, pH, solution composition, and flow rate) (Crovisier et al., 2003; Grambow, 2006; Grambow and Muller, 2001). The reaction mechanisms that govern surface or altered layer formation is critically important for understanding the weathering of silicate minerals and the biogeochemical cycling of elements. For example, researchers have suggested that the reason for the discrepancy between laboratory and field measured weathering rates is the formation of altered layers on mineral surfaces (Nugent et al., 1998; Ruiz-Agudo et al., 2016). Furthermore, the presence of altered layers or coatings on mineral surfaces affects a variety of microscopic processes (e.g., adsorption, ion diffusion, growth, dissolution, precipitation, and interfacial redox reactions) that represent the underlying phenomena controlling element cycling and radionuclide mobility in natural and engineered systems.

For borosilicate glass used as the host matrix for nuclear waste, a major component of the repository safety case is to demonstrate the ability to describe radionuclide release from the vitrified matrix over geologic time scales. Development of models that accurately predict the stability life-time and quantifying radionuclide release from glass has proven elusive because of the uncertainty surrounding both the role of the altered layer and the mechanisms that govern its development (Gin et al., 2013; Pierce et al., 2014a; Vienna et al., 2013). Pierce et al. (2014a) defines the altered layer (i.e., amorphous hydrated surface layer and crystalline reaction products) as a complex region, both physically and chemically, sandwiched between two distinct boundaries—pristine glass surface at the inner most interface and aqueous solution

ACCEPTED MANUSCRIPT

at the outer most interface. For a historical perspective and a detailed description of the models used to predict the long-term weathering of glass see Pierce et al.(2014a) and the references contained therein.

Recent advances in analytical techniques—such as time-of-flight secondary ion mass spectrometry (ToF SIMS), atom probe tomography (APT), scanning transmission electron microscopy electron energy loss spectroscopy (STEM-EELS), and energy filtered transmission electron microscopy (EFTEM)—are providing unprecedented insight into the physico-chemical properties of the altered layer and the elemental profile of the pristine glass-altered layer interface. These new insights have led investigators to question the validity of the leaching mechanism as the prevailing theory that best describes glass alteration in silica saturated solutions. The leaching mechanism and interfacial dissolution-reprecipitation mechanism (IDPM) are described briefly below.

Leaching mechanism: The leaching mechanism occurs via a set of coupled physico-chemical processes that include (i) the selective removal of charge compensating cations in the glass (i.e., exchange of H^+ or H_3O^+ for alkali or alkaline earth cations) to form an interdiffusion layer (Bunker et al., 1983; Gin et al., 2016; McGrail et al., 2001; McGrail et al., 1986; Neeway et al., 2016), (ii) protonation and rupture of bridging bonds (e.g., Si– O– Si, Si– O– Al) (Abraitis et al., 2000; Icenhower et al., 2008; Pierce et al., 2004; Pierce et al., 2010; Pierce et al., 2008a; Pierce et al., 2008b), and (iii) reconstruction of the silica network (i.e., repolymerization, condensation, or both) to form the amorphous hydrated surface layer that has a different structure and reactivity than the parent material (Bunker, 1994; Bunker et al., 1986; Bunker et al., 1988; Hopf et al., 2016; Pederson et al., 1986). The thickness, chemical composition, and pore structure of the amorphous hydrated layer changes as a function of glass composition, pH, temperature, and bulk fluid composition (Cailleteau et al., 2008; Cailleteau et al., 2011; Gin et al., 2012). Lastly if given sufficient time, crystalline alteration products (i.e., clay or zeolite) will form at hydrated layer-fluid interface and impact both the thickness and composition of the hydrated layer and, ultimately, the rate of glass corrosion (Crovisier et al., 2003; Fournier et al., 2014; Gin et al., 2012; Guittonneau et al., 2011; Pierce et al., 2007; Pierce et al., 2014a; Pierce et al., 2006).

ACCEPTED MANUSCRIPT

Interfacial dissolution-reprecipitation mechanism (IDPM): The IDPM is defined as the congruent dissolution of the glass matrix, which is spatially and temporally coupled to amorphous silica precipitation at an inward-moving reaction front (Geisler et al., 2010; Geisler et al., 2015; Hellmann et al., 2015; Putnis, 2015). In comparison to the leaching mechanism, which states the altered layer forms by the repolymerization of partially bound elements at the glass-fluid interface after the selective removal of certain elements, the IDPM conceptual model suggest that all bonds are broken at the glass-fluid interface followed by the immediate precipitation of the altered layer from a supersaturated thin-film of water at the glass-fluid interface.

The IDPM was initially proposed for glass by Geisler et al. (2010). Geisler and colleagues (2010) used a combination of ^{18}O and ^{26}Mg isotope tracer experiments in conjunction with ToF-SIMS measurements to conclude that the altered layer formed at 150°C and an initial pH ~0 were best described by the IDPM. Although the acidic pH conditions used in the experiments by Geisler et al. (2010) were not reflective of the conditions expected for a geologic repository, the results challenged the status quo. Another group conducted follow-on experiments under more realistic conditions with the SON68 glass—the French high-level waste glass composition—in deionized water at 50 °C for up to 7 months (Hellmann et al., 2015). Hellmann et al. (2015) characterized lamella removed from reacted glass coupons with high resolution nanometer scale techniques—APT, ToF-SIMS, and EFTEM—and concluded that the glass-altered layer interface was sharp, with chemical gradients in the nanometer to sub-nanometer range. Hellmann et al. (2015) concluded that their observations were consistent with the IDPM and in agreement with findings by Geisler et al. (2010; 2015).

Recently, the group at CEA Marcoule in France performed numerous studies on SON68 and the international simple glass (ISG) with the goal of resolving the debate on the mechanisms that govern the formation of the interface between the altered layer and pristine glass (Gin et al., 2017; Gin et al., 2015; Gin et al., 2016). First Gin and colleagues (2016) repeated the study performed by Hellmann et al. (2015) and concluded that the rate limiting step controlling glass alteration under silica saturated conditions is the

ACCEPTED MANUSCRIPT

accessibility of water molecules to the pristine glass surface. Gin et al. (2017; 2015) also used ISG, a six-oxide borosilicate glass reference material (Gin et al., 2013), to reduce the complexity in data interpretation cause by the formation of crystalline alteration products (i.e., clay or zeolites). ISG studies conducted in deionized water under silica saturated conditions allows researchers to focus on the impact the amorphous hydrated layer has on the rate of glass corrosion by minimizing the likelihood of crystalline alteration phases forming because both the glass and leaching solution are devoid of minor elements (e.g., Fe, Mg, Zn, etc.) required for the formation of crystalline alteration products. Gin et al. (2017; 2015) time-dependent study of the amorphous hydrated layer concluded that in the absence of crystalline alteration products that consume silicon and aluminum from the inter-diffusion and hydrated layer, the rate-limiting step in glass dissolution was the formation of a layer (i.e., passivating) that limited transport to and from the glass interface. Additionally, Gin and colleagues (2017) acknowledge that mobile cations (i.e., B, Na, and Ca) at the interface between the pristine glass and altered zone is sharp in APT measurements as observed by Hellmann et al. (2015), but the authors imply the observed sharp chemical gradient may result from measurement artifact caused by changes in the field evaporation rate for the multi-layered structure (i.e., glass, passivating layer, oscillatory hydrated layer, and clay layer). The aforementioned minor observation in the Gin et al. (2017) study is important because (1) it is consistent with previous observations (Gin et al., 2015; Hellmann et al., 2015) and (2) it suggest that the element profiles at the glass-altered zone interface may appear artificially sharper than reality in APT measurements. Lastly, Gin and colleagues (2017) proposed that the hydrated glass layer and passivating layer are separated by a rough interface from which mobile cations in the glass dissolve congruently when in contact with water and thus the leaching mechanism and IDPM were conceptually simple and could not fully explain the complexity associated with the formation of the elemental profiles observed at the glass-altered layer interface. The data central to the aforementioned conclusion and the ones by Hellmann et al. (2015) and Geisler et al. (2010; 2015) are the elemental profiles and isotopic exchange results, but very little, if any, data was collected on the structure and pore size of the altered layer.

ACCEPTED MANUSCRIPT

Lastly, the first-order approximation model developed by Wang et al. (2016) provides additional evidence that feedback between dissolution-induced cation release and cation enhanced dissolution kinetics can enable sharp dissolution fronts, leach layers, and oscillatory dissolution behavior (e.g., concentric banding observed in samples). The conclusions by Wang et al. (2016) are consistent with the experimental observations by Schalm and Anaf (2015, 2016) and Lenting et al. (2015) which describes the concentric banding observed in altered glass layers as variations in the random packing of silica nanoparticles, presumably caused by abrupt changes in key parameters (e.g., pH or dissolved cations) that impact the reaction mechanisms. In summary, these results suggest an alternative conceptual model may be needed in order to accurately describe the complexity of altered layer formation and its influence on water accessibility to the pristine glass interface.

The aim of the current study is to determine the mechanical properties of the altered layer and to correlate these physical properties to observed chemical variations. An additional objective was to relate the structure of the amorphous hydrated layer to the transformation processes that occur to silica during diagenesis. To our knowledge this is the first time this has been done. Finally, we place these results in context of by providing additional mechanistic insight in to the paradox on the processes that govern altered layer formation. To accomplish the aforementioned objectives, we have monitored the time-dependent changes in elemental release for an experiment conducted under hydraulically unsaturated conditions. The unsaturated conditions used in this study are more consistent with the open flow and transport conditions expected in a geologic repository in comparison to traditional static experiments. The experiment was performed with a multi-component borosilicate glass sample (LAWB45) at a high surface area-to-volume ratio (~200,000 m^{-1}) and 90 °C for 1.5-years and resulted in the formation of a thick altered layer (Pierce et al., 2007; Pierce et al., 2006). The formation of thick altered layers offer the opportunity to relate layer thickness and chemical composition with observed changes in elemental release by analyzing the bulk solution chemistry and characterizing the reacted glass postmortem. A unique set of analytical methods with high spatial resolution were used to characterize reacted glass

ACCEPTED MANUSCRIPT

grains postmortem to assess chemical gradients at the pristine glass-hydrated layer interface and hydrated layer-clay interface. Additionally, we highlight first-of-a-kind characterization measurements using a novel atomic force microscopy mode (PeakForce Quantitative Nanomechanical Property®) to estimate the mechanical properties of the altered layer. Based on the results presented, we propose that the glass-altered layer interface is rough, the structure and mechanical properties of the hydrated layer are consistent with a porous gel, and the elemental distribution with in this porous gel suggest the removal of molecular units. Here we propose that the removal of molecular units create a hydrated layer that closely resembles opal-AG (gel-like) and represents a random packing of aggregated sub-nanometer silica-rich particles (~0.7 nm) that are smaller than the critical nucleus for silica nanoparticles (~1.4 to 3 nm).

2 EXPERIMENTAL DETAILS

2.1 Glass Chemistry and Preparation

The development (Muller et al., 2001), production, and characterization (density, chemical composition, etc.) for the LAWB45 glass used in this study has been described previously in Pierce et al. (2008b). The LAWB45 glass is comprised of 47.86 wt% SiO_2, 12.34 wt% B_2O_3, 6.13 wt% Al_2O_3, 6.63 wt% CaO, 6.50 wt% Na_2O, 5.26 wt% Fe_2O_3, 4.62 wt% Li_2O, 3.15 wt% ZnO, 3.15 wt% ZrO_2, 2.97 wt% MgO, and 1.30 wt% others. See Table SI1 for the chemical composition in mole percent (mol%) along with the composition of other well studied glasses, specifically the French in-active high-level waste glass SON68 and the international simple glass (ISG). This comparison suggests that the difference in glass composition between SON68 and LAWB45 is in the minor components, as evidenced by ~90 mol% for each glass being composed of SiO_2,(50 mol%), B_2O_3 (>11 mol%), Al_2O_3 (~3.5 mol%), ZrO_2 (1.5 mol%), and alkali and alkaline-earth elements (>21 mol% as Na_2O, Li_2O, and CaO). The ISG glass, six oxide glass that is a simplified version of SON68, is also comparable to LAWB45 in terms of alkali and alkaline-earth content (~18 mol% for ISG), Al_2O_3 (3.8 mol%), and ZrO_2 (1.7 mol%). Although the B_2O_3/SiO_2 ratio for ISG (0.27), SON68 (0.27), and LAWB45 (0.22) are similar, ISG has a significantly higher fraction of SiO_2 (60.2 mol%) and B_2O_3 (16 mol%) in comparison to SON68 and LAWB45.

ACCEPTED MANUSCRIPT

The glass was prepared by crushing sub-samples in a ceramic ball mill. After sieving the crushed glass into <420 to >250 µm size particles (<40 to >60 mesh fraction), the sample was washed and sonicated in 18 MΩ-cm deionized water (DIW) numerous times, triple rinsed in ethanol, and then dried in a 90 °C oven (ASTM, 1994). The sieved and cleaned glass grains were stored in sealed containers containing $CaSO_4$ desiccant prior to use.

2.2 Pressurized Unsaturated Flow Test Method and Effluent Solution Analyses

The PUF system and test methods have been described previously by McGrail et al. (1996; 1999) and Pierce et al. (2011; 2007; 2014b; 2006), therefore to limit duplication only details pertinent to this experiment are discussed here. The PUF system consists of a 7.62-cm (7.62×10^{-2} m) long and 1.91-cm (1.91×10^{-2} m) diameter column fabricated from polyetheretherketone (PEEK) and has a total volume of 21.73 cm^3 (2.17×10^{-5} m^3). Prior to initiating the experiment, the PEEK column was filled with 28.51 g of cleaned LAWB45 glass, which resulted in a fill volume of 19.73 cm^3 (1.97×10^{-5} m^3). The experiment was conducted with a gap (~0.7-cm long gap [volume = 1.99 cm^3 (1.99×10^{-6} m^3)]) located near the column inlet. The mass difference between the packed and empty column was used to calculate an initial porosity of 0.458 ±0.03. The packed column was connected to the PUF system, then vacuum saturated with DIW, gradually heated to 90 °C, and allowed to gravity drain. The flow rate was set to 2 mL/d (2.31×10^{-11} m^3/s) and the DIW influent reservoir was maintained at ambient temperature and periodically refilled during the test. It is important to note that PUF experiments are advection dominated, evident by a Péclet (P_e) number of 40.3 for this experiment. The P_e calculation used an average volumetric water content (ψ) of 0.154 ±0.003 and a molecular diffusion coefficient of water of 1.0×10^{-9} m^2/s.

In-line sensors were used to constantly monitor the change in column mass, effluent pH, and electrical conductivity (Ω) over the test duration. Column mass change was used to estimate the time-dependent changes in volumetric water content (ψ). Measurements were taken as frequently as every minute and as long as every hour, resulting in a large data set for each sensor. Given the measurement frequency and noise in the sensory data, the results were smoothed using a bi-square weighting method

ACCEPTED MANUSCRIPT

where the smoothed data point, y_s, is given by $y_s = (1-\omega^2)^2$. The pH and electrical conductivity sensor are located outside of the column and thus the reported values are at or near room temperature. Additionally, effluent solution samples were collected in tared vials from which samples were extracted and acidified with high-purity concentrated HNO_3 for elemental analysis (Al, B, Ca, Fe, Li, Mg, Na, S, Si, Zn, and Zr) with inductively coupled plasma-optical emission spectroscopy (ICP-OES).

2.3 Normalized Concentration and Quantification of Elemental Release Rates

Briefly, the normalized concentration (NC_i) was calculated from the elemental concentrations in the effluent solutions with Eqn. 1

$$NC_i = \frac{(c_{i,L} - \bar{c}_{i,b})}{f_i} \tag{1}$$

where $c_{i,L}$ is the effluent solution concentration of element i (mg/L), $c_{i,b}$ is the average background solution concentration of element i (mg/L), and f_i is the mass fraction of element i in the glass (unitless).

The normalized release rates were calculated with Eqn. 2

$$r_i = \frac{4\varepsilon q(c_{i,L} - \bar{c}_{i,b})}{\psi S(1-\varepsilon)\rho\pi d^2 L f_i} \tag{2}$$

where r_i is the normalized release rate of element i (g/[m^2 d]), $c_{i,L}$ is the effluent solution concentration of element i (g/m^3), $c_{i,b}$ is the average background solution concentration of element i (g/m^3), d is the column diameter (m), L is the column length (m), q is the volumetric flow rate (m^3/d), S is the specific surface area (m^2/g), ε is the porosity (unitless), ρ is the glass density, f_i is the mass fraction of element i (unitless), and ψ is the volumetric water content (unitless). The volumetric water content is calculated based on the mass of a volume of water in a fixed column volume, accounting for changes in the solution density resulting from temperature changes. Error propagation was used to estimate of the 2σ experimental uncertainty for the elemental release rates. For a detailed description of the normalized concentration, normalized release rate, and error propagation calculations for PUF experiments see McGrail et al. (1996) and Pierce et al. (2011; 2007; 2014b; 2006).

ACCEPTED MANUSCRIPT

2.4 X-ray Diffraction and Scanning Electron Microscopy Characterization of Reacted Glass

After 530 days (~1.5 year), the PUF experiment was terminated. Upon termination, the reacted solids were sub-sampled as found (loose and moist particles) as a function of depth (1 to 2 cm intervals). The sub-samples were placed in tared sample vials, dried at room temperature in a sealed container with $CaSO_4$ desiccant, and initially analyzed for secondary reaction products using X-ray diffraction (XRD). Prior to conducting XRD, subsamples of reacted glass collected from each depth were ground in an agate mortar and pestle and each packed in individual XRD holders. The XRD pattern for all six samples were recorded with a Scintag® automated powder diffractometer (Model 3520) with CuKα radiation. Data were collected in the 2θ range from 2 to 65° with a scanning step of 0.04° and a counting time of 5 s per point. The data were analyzed with JADE combined with the International Center for Diffraction Data (ICDD) PDF-4 version 3.0 software.

Scanning electron microscopy (SEM) measurements with energy dispersive spectroscopy (EDS) mapping were performed with a Hitachi S4800 FEG-SEM with Bruker EDS detector. Prior to analysis, reacted grains were embedded in an epoxy resin and polished to obtain cross-sectional interfaces. The sample was then coated with carbon using a Cressington 208 sputter coater. Forty images were collected and used to determine altered layer thickness. The images were analyzed for thickness measurements of the hydrated and clay layers with NIH ImageJ (Abramoff et al., 2004; Schneider et al., 2012). On average 95 and 117 length measurements per image were taken for the hydrated and clay layers, respectively. This corresponds to a total of 6278 altered layer thickness measurements were taken on randomly selected grains and consisted of 2797 and 3481 measurements on the hydrated and clay layers, respectively. For each measurement location the fraction of each layer present (hydrated or clay) as well as total altered layer was estimated. All EDS measurements reported are considered semi-quantitative. Spectrum alignment was performed using a EDS Al+Cu calibration standard and the AlKα and CuKα peak positions. No other standards were used to perform the EDS analyses.

ACCEPTED MANUSCRIPT

2.5 Time of Flight Secondary Ion Mass Spectrometry of Reacted Glass

Time of flight secondary ion mass spectrometry (ToF SIMS) measurements were performed in both positive and negative ions detection modes using ToF SIMS-5 (ION-TOF GmbH, Germany). A pulsed 30 keV Bi^+ ion gun with current of 0.5 nA was used as the primary ion source with a focused beam spot size of ~ 100 nm and a m/Δm resolution from 50 to 150. The spectrometer was operated at a pressure of 5.8×10^{-9} mbar. Images were collected with a resolution of 256 × 256 points across a square imaging areas from 50 to 375 µm. Initial surface cleaning and depth profiling was performed over a 500 × 500 µm area using a Cs^+ ion-sputtering source operated at 1 keV and 74 nA. Mass spectra calibration (mass versus time of flight) were performed using H^+, Li^+, Na^+, K^+ and H^-, O^-, OH^-, C_2^- peak positions for positive and negative detection modes, respectively. The ION-TOF SurfaceLab software was used for both data acquisition and post-processing. Negative (O^-, OH^-, and C^-) and positive (Zr^+, Si^+, Al^+, Mg^+, Na^+, B^+, H^+, Li^+, Fe^+, K^+, and Ca^+) ion profiles were recorded. Because the sputtering rate and ionization yield can impact the total counts measured for each element or molecule, all elemental profiles were normalized to Zr to account for any matrix affects caused by the differences between the glass and altered layer.

2.6 Scanning Transmission Electron Microscopy Characterization of Reacted Glass

Focus Ion Beam (FIB) coupons of the altered LAWB45 glass samples were prepared by lift-out techniques from the epoxy resin cross-sectional polished SEM samples using a Hitachi NB5000 dual-beam FIB-SEM. The polished samples were carbon coated with a thick layer of carbon. A 3 µm wide by about 15 µm long tungsten cap was deposited on the cross-sectional edge of the altered LAWB45 glass samples with the long direction perpendicular to the glass edge. After lift-out the samples were mounted on an Omniprobe lift-out TEM grid and further thinned using a Ga ion beam. In the final thinning process the sample was thinned at ± 2° in order to make thinner sections at the bottom suitable to EELS and EFTEM while the top regions were left thicker for EDS mapping.

ACCEPTED MANUSCRIPT

STEM imaging (bright field and dark-field) and EDS mapping were performed using a Hitachi HF3300 cold field emission S/TEM at an accelerating voltage of 300 keV equipped with a Bruker XFlash EDS silicon drift detector. Atomic weight percents were calculated using the P/B - ZAF method with Bruker's Esprit 2.0 software. Copper was used for the energy position calibration. A TEM background was utilized with background points picked using the interactive data fit option. A series fit was chosen for the peak deconvolution method. A tile size of 2 × 2 pixels was chosen for peak deconvolution resulting in a 512 × 384 pixel image for each elemental EDS map. Selected-area electron diffraction (SAED) measurements were also performed on regions of the FIB lamella (e.g., clay and hydrated layers). The camera length used to collect the SAED images of the clay and hydrated layers were calibrated against an aluminum diffraction standard obtained from Ted Pella. Based on this measurement, the current instrument calibration had less than 1% error compared to the aluminum standard d-spacings, therefore calibration corrections to the SAED were not performed.

2.7 Electron Energy Loss Spectroscopy:

A DualEELS spectrum images (EELS-SI) were obtained using a Hitachi HF-3300 cold field emission S/TEM equipped with a Gatan Quantum GIF. Two STEM EELS spectrum images were acquired. The first consisted of 512 × 512 pixels with a spatial resolution of 2 nm/px and 2048 channels/spectrum at each pixel with an energy dispersion of 0.1 eV. A vertical binning of 130× was used to increase signal-to-noise and to decrease acquisition time. The zero-loss (-20 eV to 184.8 eV) and core-loss (89.19 eV to 276.49 eV) regions were simultaneously acquired with dwell times of 1×10^{-5} sec/px and 0.1 sec/px respectively using the DualEELS capabilities of the spectrometer. Total spectrum image acquisition time was about 2 hours. Drift corrections were applied at the end of each row with the drift correction image area chosen with a prominent feature that was stable under the electron beam. Typical maximum energy resolution of 0.7 eV was obtained as indicated by the FWHM of the zero-loss peak (ZLP). The second spectrum image consisted of 151 × 69 pixels with a spatial resolution of 3 nm/px and 2048 channels/spectrum at each pixel with an energy dispersion of 1 eV. The energy resolution at this

ACCEPTED MANUSCRIPT

dispersion was about 3 eV as measured from the ZLP. A vertical binning of 26× was used resulting in a total acquisition time of 49 minutes. All processing of the EELS-SI's was performed using DigitalMicrograph 3.0. The energy positions were calibrated for both the zero-loss and core-loss regions using the zero-loss peak maximum at each pixel. A 1st-order log polynomial background was used to better model the background of the Si-L and B-K peaks close to the sample Plasmon peak while a power law background was used for the Al-K, Si-K, and Zr-L edges which are far in energy from the Plasmon peak. The smaller spectrum image was processed using the Elemental Analysis tool built into Digital Micrograph 3.0 to extract the elemental signal intensities. Each region (Al-K, Si-K, and Zr-L) was fit using a power law background model with a Hartree-Slater Cross-section model built into the software to model the peak shapes. Plural scattering was also accounted for using the ZLP calibrated low-loss SI. The energy-loss near edge structure (ELNES) regions were included in the calculation.

Relative thickness maps were extracted and plotted as thickness (t) divided by the mean-free path (λ) (Fig. SI1a). Thicker regions of the sample result in increased inelastic scattering and multiple scattering (greater plasmon intensity and multiple plasmon peaks) and a decrease in the zero-loss peak (ZLP) intensity (Fig. SI1b). This decrease of the ZLP must be taken into account when looking at regions of significantly different relative mean free paths (t/λ). The Fourier-ratio method was used to remove the effects of multiple scattering by deconvoluting the core-loss peaks (Fig. SI2a). After deconvolution, the extracted elemental peak intensities are normalized relative to the ZLP peak intensities at each pixel of the map (Fig. SI2b). The core-loss spectrum image was background subtracted and deconvoluted by the Fourier-ratio method using the zero-loss spectrum image to remove the effects of inelastic scattering on the peak intensities. The intensity of the zero-loss peak (-2.6 to 2.5 eV) and the relative thickness was also mapped. The peak area intensities for Si (102.7 to 122.8 eV) and B (190.3 to 210.4 eV) were extracted and mapped. Line profiles of extracted maps were obtained using ImageJ.

Additionally, zirconium TEM EELS measurements of the hydrated layer were obtained using a Hitachi HF-3300 cold field emission S/TEM equipped with a Gatan Quantum GIF. The 2.5 mm high-

ACCEPTED MANUSCRIPT

resolution EELS entrance aperture of the GIF Quantum spectrometer was used with a 0.1 eV dispersion, 1 s exposure time, with 25 summed frames resulting in a 25 s total integration time for the spectrum acquisition. MathCAD was used to perform a nonlinear least squares fit (Levenberg-Marquardt method), an arctangent background correction, and two Lorentzian peaks were used to deconvolute to the Zr $L_{2,3}$ edge in the EELS spectrum.

2.8 Nanomechanical Measurements of Reacted Glass

Quantitative Nanomechanical Peak Force (PF-QNM) TappingMode™ atomic force microscopy (AFM) measurements were used to obtain images of the altered layer and to simultaneously semi-qualitatively estimate the nanomechanical properties. The initial concept is described in Hopf and Pierce (2014) with the goal of applying the approach to altered glass. PF-QNM AFM images were collected with a Bruker Multimode 8 AFM using a Nanoscope V controller, a J "vertical" scanner, and an RTESPA aluminum coated etched silicon probes, which had nominal length, cantilever spring constant, and resonance frequency 125 μm, 40 N/m, and 300 kHz, respectively. Aluminum reflective coating was placed on the backside of the probe to increase measurement sensitivity during tip sample interaction. Bruker's Nanoscope 8.15 software was used for data acquisition and analysis. Similar to the procedure described by Eskelsen et al. (2014), all new probes were dulled by scanning on commercially available sapphire standard prior to measurements. The radius of each tip was estimated to be ~13 nm by scanning a commercially available titanium roughness standard with Bruker's ScanAsyst®. Both a HOPG standard and sapphire standard was used for deflection sensitivity calibration at 2 V deflection set point.

All measurements were performed inside an acoustic dampening box that included an elastic cord isolated platform. Collectively this system minimized artifacts caused by external vibrations. All images were flattened using a zero-degree line-wise fit and an average profile global fit using Scanning Probe Image Processor (SPIP™) software version 6.3 (Metrology, 2014).

ACCEPTED MANUSCRIPT

3 EXPERIMENTAL RESULTS

3.1 PUF Test Experimental Results

Fig. SI3 shows the results collected from each in-line sensor (volumetric water content [ψ], pH, and electrical conductivity [Ω]) with the individual data points and lines representing the sensors and smoothed data, respectively. The average ψ increased from 0.145 ±0.002 during the first 250 days to 0.179 ±0.122 the last 250 days. Unlike ψ, the pH gradually decreased from 9.7 to 8.5 during the first 300 days and settled to an average value of 8.8 ±0.1. The electrical conductivity (Ω) gradually increased from 10 to 1140 μS/cm in the first 100 days, increasing to a high 4252 μS/cm on day 200 and decreasing to range from 450 to 1000 μS/cm for the remainder of the test duration. Abrupt periodic spikes in ψ near days 300 and 450 correspond to situations where the effluent line plugged.

Fig. 1. illustrates the normalized effluent concentration (NC_i) and normalized dissolution rate (r_i) as a function of time. The NC_i was calculated using Eqn. 1. The results show that Al, Ca, Fe, Mg, Zn, and Zr are being released 100 to 1000 times slower than B, Li, Na, and S (Fig. 1. a). Conversely, Si is being released 5 to 10 times slower than B, Li, Na, and S. These results suggest that B, Li, Na, and S are not being retained in the column, where as Al, Ca, Fe, Mg, Si, Zn, and Zr are being retained. Measured concentrations for Fe (50 μg/L), Mg (250 μg/L), Zn (125 μg/L), and Zr (50 μg/L) were all below detection limits and therefore are excluded from Fig. 1. a. Fig. 1. b illustrate a constant dissolution rate, evident by the average B dissolution rate after the first 100 days being in the experimental error of the average dissolution rate for the last 100 days. The observed dissolution rate spikes shown in Fig. 1. b; which occur near day 310, 430 and 530, are related to observed deviations in the volumetric water content. Similar to the normalized concentration data, the average glass dissolution based on Al and Ca release are three-orders of magnitude slower than dissolution rates based on B, Li, Na, and S. These results suggest LAWB45 glass is corroding at 0.076 ±0.007 g/(m^2·d), based on B release, which is between 2.9 and 10 times lower than the forward dissolution rate for LAWB45 (r_B = 0.22 ±0.03 g/[m^2·d] at 90 °C and pH(T) = 7.7, r_B = 0.54 ±0.07 g/[m^2·d] at 90 °C and pH(T) = 8.5, and r_B = 0.84 ±0.11 g/[m^2·d]

ACCEPTED MANUSCRIPT

at 90 °C and pH(T) = 10.1) measured under dilute conditions in single-pass flow-through (SPFT) experiments (Pierce et al., 2008b). Additionally the average dissolution rate, based on B release (r_B = 0.011 ±0.002 g/[m^2·d] at 90 °C and pH(T) = 7.7) for the LAWB45 glass was measured under silica saturated conditions in SPFT experiments and is 6.9 times slower than the value measured in the PUF experiment (Pierce et al., 2004). The B release rate measured in the PUF test corresponds to an average rate of ~10 ±1 μm/yr and suggest that ~17 % of the glass has corroded over the 1.5-year period at 90 °C in the PUF systems. The average rate is an order of magnitude greater than the rate measured for LAW-AN102 (1.4 ±0.4 μm/yr) (Pierce et al., 2006) in the PUF system after 350 days of testing at 90°C.

3.2 Post-Test Subsampling and Analysis

As shown in Fig. SI3, ψ gradual increases from day 300 until test termination. This has been observed in previous PUF experiments and correlates with pore-scale changes caused by the formation of hydrated alteration phases (e.g., clay and/or zeolithic phases) that impact the columns water-retention characteristics (McGrail et al., 1998). Therefore, upon termination of the experiment, reacted glass grains were subsampled as a function of depth every ~1 to 2 cm (0.01 to 0.02 m) and placed in individual plastic vials (Fig. SI4). The samples were analyzed for moisture content, by drying in a vacuum desiccator containing the desiccant $CaSO_4$. The weight for each vial was recorded before and after being placed in the desiccator to gravimetrically estimate the mass of water associated with each subsampled region. The most significant mass change, 1.2 grams, was observed for the two subsamples taken at the top and base of the column. Mass change for the remaining five subsamples taken from the central region gradually decreased from 0.6 to 0.2 grams until reaching the base. Aliquots of dried reacted grains from each vial were sampled and analyzed for secondary reaction products using bulk X-ray diffraction (XRD).

Bulk powder XRD results suggest the greatest extent of alteration occurred near the column inlet, evident by the intense reflection at 6° 2θ for subsample LAWB45-1 in comparison to the other five subsamples (see Fig. SI4 in the supporting information). This subsample also showed reflections at 19.8 and 61.3° 2θ. These are characteristic reflection for a 14 Å clay mineral and closely resembles a

ACCEPTED MANUSCRIPT

phyllosilicate phase, such as nontronite ($Na_{0.3}Fe_2Si_4O_{10}[OH])_2 \bullet 4H_2O$), which is an iron rich smectite clay phase. The characteristic phyllosilicate reflections were also observed in the other five subsamples. A high-resolution TEM (HRTEM) image of the mixed alkali/alkaline-earth phyllosilicate phase is shown in Fig. 2 along with an inset of the fast-fourier transform of the HRTEM image. These results and the selected-area electron diffraction (SAED) data confirm the formation of a mixed alkali/alkaline earth phyllosilicate phase. The presence of the alkali/alkaline earth phyllosilicate observed in this study is consistent with data collected on the influence of alkali and alkaline-earth elements on glass dissolution and subsequent phyllosilicate formation (Aréna et al., 2016; Fleury et al., 2013).

Based on the results from XRD and the moisture content analyses as well as previous PUF experiments conduct with similar glass compositions [see Pierce et al. (2011; 2007; 2014b; 2006)], the LAWB45-1 subsample was selected for more detailed characterization.

3.3 Reacted Glass Altered Layer Thickness

A combination of imaging techniques, scanning electron microscopy (SEM) and atomic force microscopy (AFM), were used to determine the altered layer thickness on epoxy mounted cross-sectioned glass grains. These images were also used to estimate the percentage of the hydrated and clay layers that contribute to the total altered layer thickness.

For the SEM measurements, approximately forty images that ranged in scan size between 3 and 260 μm were collected and analyzed. A secondary electron SEM image of cross-sectioned LAWB45-1 reacted grains are shown Fig. SI5 and SI6 along with identification labels for various components in the image (i.e., glass [G], hydrated layer [H], clay layer [C], and epoxy [E]). These representative images illustrate that the altered layer thickness varies from grain to grain; as evident by the altered layer thickness minimum and maximum range based on all 40 images of 0.64 μm and 61 μm, respectively (Table 1). The large variation in minimum and maximum results from the grain to grain variability (i.e., heterogeneous distribution) in the layers presence and is likely the result of certain inter-grain pores (i.e., macro-pores between glass grains) in the column transmitting more water than others and resulting in

ACCEPTED MANUSCRIPT

certain glass grains developing thicker altered layers. This observation is consistent with previous PUF experiments that also show a heterogeneous distribution in the thickness of the altered layer for different grains of reacted glass (Pierce and Bacon, 2011; Pierce et al., 2007; Pierce et al., 2014b; Pierce et al., 2006). Collectively, the SEM image analyses suggest an average altered layer thickness of 13.2 ±8.3 μm with the hydrated and clay layer representing 74.8% and 25.2% of the total altered layer, respectively. Dividing the value for the hydrated layer by the experimental duration (~1.5 years) results in an alteration rate estimate of 6.6 ±4.1 μm/yr; which is within the experimental error of the value estimated from the B release rate data (~10 ±1 μm/yr).

In addition to SEM, AFM images were also collected on the cross-sectioned LAWB45-1 subsample. The purpose of the AFM measurements was to corroborate the SEM thickness measurements. Nine AFM images were used to determine altered layer thickness, which includes the hydrated and clay layers (see Fig. SI7). For each image several measurements per image of layer thickness, 14 on average, were taken. The number of measurements was based on the fraction of the altered layer contained in any single image. Similar to the SEM images, the AFM images illustrated the heterogeneous distribution of altered layer formed on the glass surface. The average altered layer thickness was 16.1 ±5.5 μm, with the hydrated and clay layer accounting for 77% and 23% of the total altered layer thickness. The estimated corrosion rate based on AFM measurement of the hydrated layer is 8.3 ±2.8 μm/yr, which is within the experiment error of the value estimated from SEM and the B release rate data.

3.4 Reacted Glass Altered Layer Chemical Composition

The chemical composition of the altered layer was determined using a combination of SEM with energy dispersive spectroscopy (EDS), time-of-flight secondary ion mass spectrometry (ToF-SIMS), and scanning transmission electron microscopy (STEM) with EDS. The SEM-EDS and ToF-SIMS measurements were used to provide micrometer scale insight into the element distribution and chemical composition of the altered layer; while the STEM-EDS was used to gain nanometer scale insights on the

ACCEPTED MANUSCRIPT

chemical complexity of the altered layer. Additionally, the ToF-SIMS measurements provide details on H^+, OH^-, and Li^+ which cannot be obtained with EDS.

3.4.1 Scanning Electron Microscopy – Energy Dispersive Spectroscopy

Shown in the SEM-EDS results are a combination of spot and line profiles that were used to determine the chemical composition of the altered layer. The results for a representative grain from the cross-sectioned LAWB45-1 sample are shown in Fig. SI6. These data illustrate that the pristine glass (146.9 μm) is chemically distinct from the hydrated layer (34.4 μm), clay layer (15.6 μm), and epoxy layer (111.0 μm) (Fig. SI6). The line profile shows the following general trends in element atomic % moving from the pristine glass edge to the edge of the epoxy layer: (1) a decrease in Al, Ca, K, and S, (2) a gradual decrease followed by a spike in Fe, Mg, O, Si, and Zn in the clay layer, (3) a sharp decrease in Na followed by a spike in the clay layer, and (4) an increase in Zr in the hydrated layer followed by a sharp decrease (Fig. SI6a). Results from spot analyses, suggest the hydrated layer is mainly composed of Al, Ca, O, Si, and Zr, whereas Al, Mg, O, Si, and Zn are the main components of the clay layer (Fig. SI6 b and c). It's important to note that light elements (Li, B, or H) cannot be detected by EDS. Hydrated layers with similar chemical composition have been observed in previous studies with multi-component glasses corroded at high S/V (Gin et al., 2012; Gin et al., 2011; Guittonneau et al., 2011; Rajmohan et al., 2010).

3.4.2 Time-of-Flight Secondary Ion Mass Spectrometry

ToF-SIMS measurements were performed to obtain Li^+, B^+, and H^+ profiles in the positive ion mode and OH^- in the negative ion mode (

Fig. 3..). Results show that Li is significantly enriched in the clay layer evident by the Li^+ profile being correlated with Mg^+ and Fe^+ profiles, which are consistent with the Mg and Fe SEM-EDS results. Furthermore, the H^+ and OH^- profiles are anti-correlated with that of the B^+ profile for the region that spans from the hydrated layer to the unaltered glass. Additionally, these data confirm the following: (a)

ACCEPTED MANUSCRIPT

the concentration of Si and Al is nearly constant throughout the altered layer with Al being enriched slightly in the clay layer, (2) the H profile is anti-correlated with the B profile, (c) the hydrated layer is mainly composed of Al^+, Ca^+, H^+, K^+, Si^+, and Zr^+, and (d) the clay layer is significantly enriched in Fe, Mg, and Li.

3.4.3 Scanning Transmission Electron Microscopy – Energy Dispersive Spectroscopy

Two FIB sections (Fig. 4. and 5) were removed from altered glass grains in the LAWB45-1 subsample, thinned and cleaned in an Ar ion mill to a thickness of approximately 100 nm, and used for STEM-EDS measurements. It is important to note that analysis of the STEM images provided an altered layer thickness (8.1 ±0.7 μm) which is within the experimental error of the values obtained from measurements on AFM and SEM images.

The STEM-EDS (Fig. 4.) and STEM images (Fig. 4. and 5) reveal that the hydrated layer is physically and chemically complex. For example, visual inspection of the hydrated layer (Fig. 5. and Table SI2) can be further segregated into three additionally layers: (1) an alkali- and alkaline-earth depleted layer (0.3 to 0.6 μm) that is slightly depleted in Na, Zn, and Mg in comparison to the unaltered glass, (2) a region of the hydrated layer (2.6 ±0.7 μm) that is extremely porous and composed of Al, Ca, Si and Zr, and (3) a second region of the hydrated layer (2.9 ±0.9 μm) that is denser (i.e., less porous) but compositionally similar to the porous hydrated region. Lastly, two transition zones are also present within the altered layer (Fig. 5.), the first transition zone occurs between the transition from the porous to dense hydrated regions and the second from the dense hydrated region to the clay layer. The variation in hydrated layer porosity (e.g., denseness of the hydrated layer) is shown best in Fig. 5. and this change can be attributed to differences in the pore size distribution because the average intensity in the dark-field image remains relatively constant which indicates that the volume of material is consistent across the altered layer. In each case, the transition zone is ~0.2 μm thick and also illustrates a gradual shift in chemical composition. Although at different length scales, the compositional changes observed in the

ACCEPTED MANUSCRIPT

hydrated and clay layers of the FIB subsample in the STEM-EDS are similar to the SEM-EDS spectra (Table SI2).

To assess the hydrated layer elemental profiles more thoroughly, we corrected for the relative changes in atomic percent due to variations in the elemental composition of glass and hydrated layers by estimating a mass transfer coefficient (Table 2), tau (τ), for various elements (Al, Ca, Fe, Mg, Na, Si, Zn, and Zr) (Anderson et al., 2002; Brimhall and Dietrich, 1987):

$$\tau_{j,w} = \frac{C_{j,w}C_{i,p}}{C_{j,p}C_{i,w}} - 1 \quad (3)$$

where $C_{i,w}$ – concentration of immobile element in altered layer, $C_{i,p}$ – concentration of immobile element in the pristine glass, $C_{j,w}$ – concentration of element *j* in altered layer, and $C_{j,p}$ – concentration of element *j* in pristine glass. Values of $\tau_{j,w} > 0$ indicate enrichment of element *j*, $\tau_{j,w} < 0$ indicates depletion, and $\tau_{j,w} = 0$ suggests element *j* is immobile in the weathered zone with respect to the parent material. Here we use Zr as the immobile element in the weathered zone. These clearly shows that Mg ($\tau \geq -0.76$), Na ($\tau \geq -0.72$), Zn ($\tau \geq -0.77$), and Fe ($\tau \geq -0.63$) in the hydrated layer are significantly depleted relative to the immobile element Zr, evident by τ values that are less than -0.5. The τ values calculated for Ca and Si suggest very little change with respect to Zr, ranging from -0.34 to -0.48 for Ca and from -0.46 to -0.62 for Si in the hydrated layer.

In summary, the chemical composition results obtained from the SEM-EDS, ToF-SIMS, and STEM-EDS indicate that the clay layer is composed of Al, Si, and O and enriched in Li, Zn, Fe, and Mg in comparison to the glass. The hydrated layer is mainly composed of Al, Ca, H, O, Si, and Zr with a small amount of K and the layer's density varies with increasing distance from the glass. Lastly, the B profile is anti-correlated with the H profile.

3.5 Physico-Chemical Properties of the Hydrated Layer

ACCEPTED MANUSCRIPT

The results discussed in the aforementioned sections illustrate that the properties of the hydrated layer are physically and chemically complex. Unraveling this complexity by measuring key physico-chemical properties can help support the development of more accurate models for glass corrosion. Described below are the results collected using several unique nanometer-scale characterization techniques (i.e., Quantitative Nano-mechanical Peak Force® AFM and STEM imaging) to determine the mechanical properties and estimate the size of pores present in the hydrated layer.

3.5.1 Hydrated Layer Nano-mechanical Properties

Atomic force microscopy was also used to estimate the mechanical properties of the hydrated layer for the first time. Hopf and Pierce (2014) were the first to suggest applying Quantitative Nanomechanical Peak Force® (PF-QNM) to characterize the mechanical properties of the altered layer. Fig. 6 shows a representative 10 × 10 μm image with a PF-QNM pixel map resolution of 512 × 512. The PF-QNM map set includes height, Peak Force error, modulus, log modulus, adhesion, and deformation. In addition to the images, a histogram of the modulus values is also provided in Fig. 6 and shows a direct comparison of the modulus results for the bulk glass, hydrated layer, and epoxy. These results suggest the hydrated layer has a modulus that ranges between ~20 to 40 GPa, which is within the range of porous silica that contains from ~20 to ~50% porosity, but higher than densified silica xerogel (0.6 to 4 GPa) (Murray et al., 2002) and significantly lower than dense silica (~70 or 80 GPa) (Adachi and Sakka, 1990; Rimza and Du, 2014). The values obtained for the glass (40 to 80 GPa) and epoxy (~10 GPa) are within the experimental error of values measured for nuclear waste glasses and polymers with nano-indenters and illustrates the accuracy of the measurement. Previous corrosion studies that used thermoporometry and X-ray scattering to characterize the hydrated layer formed during pseudo-dynamic experiments with the multi-component R7T7 glass, showed that the hydrated layer consisted of more than 40% porosity by volume and contained pore radii that were ~4.5 nm in size (Deruelle et al., 1997). The pore radii measured by Deruelle et al. (1997) is consistent with a recent study by Gin and colleagues (2015) where they traced the penetration depth of dye molecules ~1 nm in size (i.e., bromothymol blue and methylene blue) into gels

ACCEPTED MANUSCRIPT

formed on corroded ISG surfaces and concluded that the hydrated layer behaved like a molecular seive with a pore cutoff of <1 nm in size. Additionally, Deruelle et al. (1997) showed that the porous network that formed when simplified glasses were corroded is directly related to Zr content of the glasses tested. This observation is consistent with Cailleteau et al. (2008; 2011) and suggests that the relationship between Zr content and pore network is directly related to pore clogging caused by rapid dissolution during the early stages of corrosion.

3.5.2 Estimate of Pore Sizes Present in the Hydrated Layer

The physical complexity of the hydrated layer can be observed in bright-field (BF) and dark-field (DF) TEM and STEM images (Fig. 7). Images of the honeycomb shaped region reveals what appears to be either a gel or aggregates of irregular shaped particles. Additionally, BF TEM and STEM images show a density contrast in sample regions with similar thickness, suggesting that these regions contain localized areas consistent with a network of connected and unconnected voids. To further evaluate this observation, 2D STEM images were segmented to obtain a qualitative estimate of pore volume. The 2D DF STEM images were initially plane corrected with a global correction using an average profile fit and a third-order LMS line-wise correction in Scanning Probe Image Processor (SPIP^{TM} 6.4.2) software to reduce planar distortions. Pore analysis was performed using the threshold detection method with the threshold being auto calculated. This semi-quantitative analysis suggested that the pore volume present in the 2D segmented image is ≥ 22% and has a minimum and maximum pore size 5 and 113 nm, respectively (Fig. 8). The estimate of pore volume for this region of the LAWB45 hydrated layer is within the experimental error of porosity values obtained for natural opal-A samples, which have pore volumes that range from 23 to 28% (Eckert et al., 2015). It should be mentioned that setting the threshold limits for the TEM image is somewhat arbitrary because of the 3D gray contrast through various thicknesses. Although this is an estimate, the values are consistent with the Young's modulus measurement discussed above. Previous studies have also suggested pores present in the hydrate layer are between <1 and 100 nm (Deruelle et al., 1997; Gin et al., 2015) and may restrict transport and movement of solutes from the glass interface to the

ACCEPTED MANUSCRIPT

bulk solution. In summary, the results presented illustrate the porous nature of the hydrated layer; however additional techniques, such as electron tomography, will be required to quantify the layers porosity and pore size distribution.

4 DISCUSSION

4.1 Zirconium Coordination in the Hydrated Layer

The SEM-EDS and STEM-EDS measurements illustrate that Zr is enriched in the hydrated layer and absent from the clay layer. The retention of Zr in the hydrated layer offers insight in to the processes that govern hydrated layer formation and is consistent with observations from previous studies with Zr-containing multi-component borosilicate glasses. For example, Jollivet et al. (2013) and Pèlegrin et al. (2010) used X-ray absorption spectroscopy measurements to probe the local coordination of Zr in unreacted and reacted glasses and confirmed that Zr is in the octahedral coordination ($^{[6]}$Zr) in both the pristine glass and altered zone and is likely charge compensated by two alkali (e.g., K) or one alkaline-earth element (e.g., Ca). Fig. 9 shows STEM-EELS maps of a thin corner of the cracked hydrated layer shown in Fig. 7**Error! Reference source not found.**a – d. These data illustrates the presence of Zr encased Al and Si-rich regions in the hydrated layer. To assess the Zr coordination in this layer, Zr TEM EELS was collected and processed similar to the approach described in Jollivet et al. (2013). The full-width at half maximum (FWHM) for the two Lorentzian peaks in the Zr $L_{2,3}$ edge spectrum were constrained to be equal, while the peak positions and intensities were allowed to relax. Shown in Fig. SI8 is a background-subtracted spectrum with the fitted peaks. Although the results have a high signal-to-noise, the deconvolution suggests that Zr is probably $^{[6]}$Zr rather than $^{[8]}$Zr in the hydrated layer. The encased features of Zr in the Al and Si-enriched regions of the Zr STEM-EELS image also suggest that the hydrated layer is devoid of Zr-bearing crystalline phases that would be more indicative of $^{[8]}$Zr oxides or silicates. One plausible explanation for these features is that Al, Si, and Zr molecular units (e.g., $^{[6]}$Zr—O—Si) remain intact after being removed from the pristine glass during the dissolution process. Recent

ACCEPTED MANUSCRIPT

studies illustrates that the progressive addition of high-valence cation, such as Hf (Hopf et al., 2016) and Zr (Bergeron et al., 2010), in borosilicate glass creates $^{[6]}$Hf—O—Si and $^{[6]}$Zr —O—Si units in the glass network that are more resistant to hydrolysis than the Si—O—Si, Al—O—Si, or B—O—Si units. Additionally, Monte Carlo simulations suggest that not only is rupture of the $^{[6]}$Zr—O—Si or $^{[6]}$Hf—O—Si bonds difficult, but these sites can also serve as the template for hydrated layer formation (Hopf et al., 2016).

4.2 Hydrated Layer Formation/Structure and Relationship To Silica Diagenesis:

Formation of sedimentary silica deposits as a result of diagenesis, whether from burial or sintering, occurs via a paragenetic sequence where hydrous amorphous silica transforms to crystalline or crypto-crystalline silica through a sequence of intermediate phase transitions (Lynne et al., 2007; Williams and Crerar, 1985). This paragenetic sequence is influenced by a variety of factors (e.g., pore-water chemistry, permeability, lithology, and surface area); however, temperature and time have the greatest influence on the transformation process. Briefly, the following structural changes occur to silica as the sedimentary deposit ages:

- hydrous amorphous silica (opal-A), which exhibits a range of structural disorder, is converted to paracrystalline opal via a dehydration reaction coupled to structural reorganization and pore-closure (Herdianita et al., 2000; Icopini et al., 2005). Opal-A can be further divided into two subgroups, opal-AG for amorphous gel-like and opal-AN for amorphous network- or glass-like (Langer and Flörke, 1972).
- paracrystalline opal undergoes additional dehydration and is eventually converted to microcrystalline quartz. Paracrystalline opal can be further categorized into opal-CT (disordered α-cristobalite, α-tridymite) or opal-C (well ordered α-cristobalite with tridymite traces) (Jones and Segnit, 1971). Microcrystalline quartz consists of aggregated silica crystallites or silica clusters.

ACCEPTED MANUSCRIPT

Here we will focus our attention on the steps involved in the formation of opal-A and the transformation from opal-A to opal-CT/-C as it is most germane to the discussion on altered layers. Evidence of the molecular-scale ordering that occurs as opal-A is transformed to opal-CT/-C is the FWHM height of the most prominent diffraction band near 4 Å (Herdianita et al., 2000; Lynne et al., 2007). This band changes from a broad peak for opal-A (FWHM = ~1.29 Å) to a more ordered peak for opal-CT/-C (FWHM from 0.47 to 0.16 Å) (Lynne et al., 2007). To assess the structure of the hydrated layer, we conducted a selected-area electron diffraction (SAED) measurement. The results from the LAWB45 FIB lamella are shown in Fig. 10 and illustrate a diffuse ring at 3.4 Å corresponding to a broad FWHM 1.75 Å (13 °2θ) amorphous band. Comparing the broad diffraction spectrum obtained for the hydrated layer to the Opal-A study by Eckert et al. (2015) suggests the hydrated layer lacks long-range order and, although similar to opal-A, the layer contains a higher degree of disorder and/or strain (

ACCEPTED MANUSCRIPT

ACCEPTED MANUSCRIPT

Table 3). Several reasons may explain the greater amount of disorder: (1) presence of cations in the structure other than Si (e.g., Al or Zr) and/or (2) a greater distribution of irregularly shaped spherules as a result of alkali/alkaline-earth cations that have exchanged for hydrogen on the silanol group. For example, Nicolau et al. (2014) proposed that attached cations, such as Ca, Na, K, and Al, contributes the higher degree of structural disorder of opal-A from El Tatio (FWHM values from 7.8 to 12.5 °2θ) (

ACCEPTED MANUSCRIPT

ACCEPTED MANUSCRIPT

Table 3). These cations replace the silanol protons (SiOH) in the silica network or form negatively charged isomorphic tetrahedra at the surface or in the amorphous structure. It is important to note that the fraction of trace elements in the El Tatio sinters is higher than typical opal deposits. The trace elements contribution in typical opal deposits is between 1 and 2 % with Al (0.5 to 1.5%), Na (0.05 to 0.2%), K (0.1 to 0.5%), and Ca (0.05 to 0.3%) being the most common (McOrist and Smallwood, 1997; McOrist et al., 1994). Thus the higher degree of disorder and/or strain observed in the hydrated layer diffraction pattern when compared to opal-AG is not surprising given the significant fraction of Al, Ca, and Zr present in the layer.

4.3 Distinct Regions Present in Hydrated Layer

Recent results collected with corroded ISG samples by Gin and colleagues (2017) suggested the hydrated layer may be composed of three sublayers: hydrated glass, rough interface (rim), and passivating layer. Hydrated glass sublayer is described as a thin region adjacent to the pristine glass interface that is hydrated but chemically almost identical to the unaltered glass. The rough interface is a region created in the early stages of the glass-water reaction and serves as an inward moving reaction front that persists throughout the glass-water reaction. The final sublayer, passivating layer, is a region where soluble cations (e.g., B, Na, and Ca) are preferentially released in comparison to network former elements (e.g., Al, Si, and Zr). To assess the possibility of additional sublayers in the LAWB45-1 FIB samples, Si and B EELS spectrum images were collected using the Si L- and B K-edges (Fig. 11). These data clearly shows the presence of ~250 nm long region that includes a rough interface and a porous zone (i.e., passivating) that can restrict transport of elements. This is further illustrated by the changes in the Si and B EELS spectrums for each sublayer.

The amorphous hydrated layer can be defined as a gel (i.e., 3D continuous network that encapsulates a liquid phase), which can be either colloidal or polymeric. Colloidal gels consist of a network built from agglomerated colloidal particles (particle diameter ~1 to 1000 nm); where as polymeric gel consist of network of aggregated sub-colloidal particles (<1 nm). Small-angle X-ray scattering experiments have

ACCEPTED MANUSCRIPT

shown that the critical nucleus for silica nanoparticles is from 1.4 to 3 nm in size (Icopini et al., 2005; Tobler et al., 2009). Thus if the hydrated layer is consistent with a colloidal gel the average crystallite size would be >1.4 nm whereas, if it is more consistent with a polymeric gel the average crystallite size would be <1.4 nm. Analysis of the SAED spectrum using the Scherrer equation suggests the particles have an average size of ~0.7 nm (Fig. 10), which is close to short-range order of 0.8 nm established for glasses, based on diffraction and spectroscopic methods (Zarzycki, 1982). This indicates that the amorphous hydrated layer may be more consistent with a polymeric gel that is composed of molecular units <1 nm in size. These molecular units are made available during the glass corrosion process and likely results from difficult to hydrolyze units, such as Si—O—Zr units. Here we propose that these molecular units aggregate together to form a 3D continuous hydrated network (i.e., gel) and the size of individual particles or molecular units is a function of formation conditions (e.g., pH, ionic strength, nano-confinement, and solute composition) in the hydrated layer (Rimer et al., 2005; Rimer et al., 2008; Rimer et al., 2007). It is this size distribution and packing density that leads to the concentric bands observed in the hydrated layer (Fig. 8a) (Schalm and Anaf, 2015, 2016). In summary, the results collected in the presented in this study indicate the hydrated layer can restrict the transport of water and solutes and thus influence the rate of glass corrosion.

5 CONCLUDING REMARKS

The IDPM conceptual model assumes that all the bonds at the interface are broken followed by the simultaneous precipitation of amorphous silica at an inward moving reaction interface as evidenced by the sharp Si and B profile at the glass-altered layer interface (Geisler et al., 2010; Geisler et al., 2015; Hellmann et al., 2015). For the borosilicate glass tested in this study, the EELS spectrum images suggest the interface is rough and can not be fully explained by either conceptual model (i.e., leaching mechanism or IDPM). The combination of the rough interface and porous nature of the hydrated layer suggest the altered layer region is physically and chemically complex and describing the evolution of this interface over time will require the incorporation of a number of complex reactions. One aspect that has not been

ACCEPTED MANUSCRIPT

considered in past model development efforts is the nano-porous nature of the altered layer and how this structure influences both solution chemistry and physical mass transport processes. A recent review by Zachara et al. (2016) highlights the importance of mass transport through internal pore domains within material, referred to as internal domains in porous media, and how these domains not only dominate the reactive surface area of materials but also represent zones that are extremely important from the stand-point of chemical reactivity and fluid storage. Transport of water and solutes in and out of these zones is characterized by slow advection and/or diffusive release. Furthermore, confined water in these zones has lower activity and mobility as a result of the formation of a partially ordered film of water on the pore walls; thus impacting ion hydration, sorption, and solid phase formation. A next step in the development of models for glass weathering is to incorporate aspects of molecular scale ordering that occurs as the hydrated gel undergoes dehydration and changes at the pore scale (i.e., silica diagenesis) and how these processes are influenced by localized changes in pH and ionic strength. The new computational model recently proposed by Wang et al. (2016) represents an initial first step in the direction of more accurately describing silicate weathering over geologic time scales.

6 ACKNOWLEDGMENTS

Portions of this research was supported by the Oak Ridge National Laboratory (ORNL) Laboratory Directed Research and Development Program, U.S. Department of Energy's (DOE) Environmental Management (EM) Tank Waste Management program, and DOE EMs Office of River Protection, Immobilization of Low-Activity Waste Program funded through Washington River Protection Solutions. ORNL is operated by UT-Battelle, LLC for the US DOE under Contract No.'s DE-AC05-00OR22725.

ACCEPTED MANUSCRIPT

7 REFERENCES

Abraitis, P., Livens, F., Monteith, J., Small, J., Trivedi, D., Vaughan, D. and Wogelius, R. (2000) The Kinetics and Mechanisms of Simulated British Magnox Waste Glass Dissolution as a Function of pH, Silicic Acid Activity, and Time in Low-Temperature Aqueous Systems. Applied Geochemistry 15, 1399−1416.

Abramoff, M., Magalhaes, P. and Ram, S. (2004) Image Processing with ImageJ. Biophotonics International 11, 36-42.

Adachi, T. and Sakka, S. (1990) Dependence of the Elastic Moduli of Porous Silica Gel Prepared by the Sol-Gel Method on Heat-Treatment. Journal of Material Science 25, 4732-4737.

Anderson, S., Dietrich, W. and Brimhall, G. (2002) Weathering profiles, mass-balance analysis, and rates of solute loss: Linkages between weathering and erosion in a small, steep catchment. Geological Society of America Bulletin 114, 1143-1158.

Angeli, F., Gaillard, M., Charpentier, T. and Jollivet, P. (2008) Influence of zirconium on the structure of pristine and leached soda-lime borosilicate glasses: Towards a quantitative approach by 17O MQMAS NMR. Journal of Non-Crystalline Solids 354, 3713-3722.

Aréna, H., Godon, N., Rebiscoul, D., Podor, R., Garcès, E., Cabie, M. and Mestre, J.-P. (2016) Impact of Zn, Mg, Ni, and Co elements on glass alteration: additive effect. Journal of Nuclear Materials 470, 55-67.

ASTM (1994) Standard Test Methods for Determining Chemical Durability of Nuclear Waste Glasses: the Product Consistency Test (PCT), American Society for Testing and Materials.

Bergeron, B., Galoisy, L., Jollivet, P., Angeli, F., Charpentier, T., Calas, G. and Gin, S. (2010) First investigation of the influence of IVB elements (Ti, Zr, and Hf) on the chemical durability of soda-lime borosilicate glasses. Journal of Non-Crystalline Solids 356, 2315-2322.

Brimhall, G. and Dietrich, W. (1987) Constitutive mass balance relations between chemical composition, volume, density, porosity, and strain in metasomatic hydrochemical systems: Results on weathering and pedogenesis. Geochimica et Cosmochimica Acta 51, 567-587.

Bunker, B. (1994) Molecular mechanisms for corrosion of silica and silicate glasses. Journal of Non-Crystalline Solids 179, 300-308.

Bunker, B., Arnold, G. and Beauchamp, E. (1983) Mechanisms for Alkali Leaching in Mixed-Na-K-Silicate Glasses. Journal of Non-Crystalline Solids 58, 295-322.

Bunker, B., Arnold, G., Day, D. and Bray, P. (1986) The effect of molecular structure on borosilicate glass leaching. Journal of Non-Crystalline Solids 87, 226-253.

Bunker, B., Tallant, D., Headley, T., Turner, G. and Kirkpatrick, R. (1988) The Structure of Leached Sodium Borosilicate Glass. Physics and Chemistry of Glasses 29, 106−120.

Cailleteau, C., Angeli, F., Devreux, F., Gin, S., Jestin, J., Jollivet, P. and Spalla, O. (2008) Insight into silicate-glass corrosion mechanisms. Nature 7, 978-983.

ACCEPTED MANUSCRIPT

Cailleteau, C., Devreux, F., Spalla, O., Angeli, F. and Gin, S. (2011) Why do certain glasses with a high dissolution rate undergo a low degree of corrosion? Journal of Physical Chemistry C 115, 5846-5855.

Crovisier, J., Advocat, T. and Dussossoy, J. (2003) Nature and role of natural alteration gels formed on the surface of ancient volcanic glasses (Natural analogs of waste containment glasses). Journal of Nuclear Materials 321, 91-109.

Deruelle, O., Barboux, P., Spalla, O., Ricol, S., Lambard, J. and Vernaz, E. (1997) Morphology of Altered Layers of Glasses, Universite d'Ete CEA Valrho pp. 394-402.

Eckert, J., Gourdon, O., Jacob, D., Meral, C., Monteiro, P., Vogel, S., Wirth, R. and Wenk, H.-R. (2015) Ordering of water in opals with different microstructures. European Journal of Mineralogy 27, 203-213.

Eskelsen, J., Qi, Y., Schneider-Pollack, S., Schmitt, S., Hipps, K. and Mazur, U. (2014) Correlating elastic properties and molecular organization of an ionic organic nanostructure. Nanoscale 6, 316-327.

Farges, F., Ponader, C. and Brown, G. (1991) Structural environments of incompatible elements in silicate glasses/melt systems. I. Zirconium at trace levels. Geochimica et Cosmochimica Acta 55, 1563-1574.

Fleury, B., Godon, N., Ayral, A. and Gin, S. (2013) SON68 glass dissolution driven by magnesium silicate precipitation. Journal of Nuclear Materials 442, 17-28.

Fournier, M., Gin, S. and Frugier, P. (2014) Resumption of nuclear glass alteration: State of the art. Journal of Nuclear Materials 448, 348-363.

Galoisy, L., Pelegrin, E., Arrio, M., Ildefonse, P. and Calas, G. (1999) Evidence for 6-coordinated zirconium in inactive nuclear waste glasses. Journal of American Ceramic Society 82, 2219-2224.

Geisler, T., Janssen, A., Scheiter, D., Stephan, T., Berndt, J. and Putnis, A. (2010) Aqueous corrosion of borosilicate glass under acidic conditions: A new corrosion mechanism. Journal of Non-Crystalline Solids 356, 1458-1465.

Geisler, T., Nagel, T., Kilburn, M., Janssen, A., Icenhower, J.P., Fonseca, R., Grange, M. and Nemchin, A. (2015) The mechanism of borosilicate glass corrosion revisited. Geochimica Et Cosmochimica Acta 158, 112-129.

Gin, S., Abdelouas, A., Criscenti, L.J., Ebert, W.L., Ferrand, K., Geisler, T., Harrison, M.T., Inagaki, Y., Mitsui, S., Mueller, K.T., Marra, J.C., Pantano, C.G., Pierce, E.M., Ryan, J.V., Schofield, J.M., Steefel, C.I. and Vienna, J.D. (2013) An International Initiative on Long-term Behavior of High-Level Nuclear Waste Glass. Materials Toda 16, 243-248.

Gin, S., Beaudoux, X., Angeli, F., Jegou, C. and Godon, N. (2012) Effect of composition on the short-term and long-term dissolution rates of ten borosilicate glasses of increasing complexity from 3 to 30 oxides. Journal of Non-Crystalline Solids 358, 2559-2570.

Gin, S., Guittonneau, C., Godon, N., Neff, D., Rebiscoul, D., Cabie, M. and Mostefaoui, S. (2011) Nuclear Glass Durability: New Insight into Alteration Layer Properties. Journal of Physical Chemistry C 115, 18696-18706.

ACCEPTED MANUSCRIPT

Gin, S., Jollivet, P., Barba-Rossa, G., Tribet, M., Mougnaud, S., Collin, M., Fournier, M., Cadel, E., Cabie, M. and Dupuy, L. (2017) Atom-Probe Tomography, TEM, and ToF-SIMS study of borosilicate glass alteration rim: a multiscale approach to investigating rate-limiting mechanisms. Geochimica et Cosmochimica Acta 202, 57-76.

Gin, S., Jollivet, P., Fournier, M., Angeli, F., Frugier, P. and Charpentier, T. (2015) Origin and consequences of silicate glass passivation by surface layers. Natue Communications 6:6360, 1-8.

Gin, S., Neil, L., Fournier, M., Frugier, P., Ducasse, T., Tribet, M., Abdelouas, A., Parruzot, B., Neeway, J. and Wall, N. (2016) The controversial role of inter-diffusion in glass alteration. Chemical Geology 440, 115-123.

Grambow, B. (2006) Nuclear Waste Glasses - how durable? Elements 2, 357-364.

Grambow, B. and Muller, R. (2001) First-order dissolution rate law and the role of surface layers in glass performance assessment. Journal of Nuclear Materials 298, 112-124.

Guittonneau, C., Gin, S., Godon, N., Mestre, J.-P., Dugne, O. and Allegri, P. (2011) A 25-year laboratory experiment on French SON68 nuclear glass leached in a granitic environment - First investigations. Journal of Nuclear Materials 408, 73-89.

Hellmann, R., Cotte, S., Cadel, E., Malladi, S., Karlsson, L.S., Lozano-Perez, S., Cabie, M. and Seyeux, A. (2015) Nanometre-scale evidence for interfacial dissolution-reprecipitation control of silicate glass corrosion. Nature Materials 14, 307-311.

Herdianita, N., Browne, P., Rodgers, K. and Campbell, K. (2000) Mineralogical and textural changes accompanying aging of silica sinters. Mineralium Deposita 35, 48-62.

Hopf, J., Kerisit, S., Angeli, F., Charpentier, T., Icenhower, J.P., McGrail, B.P., Windisch, C.F., Burton, S. and Pierce, E.M. (2016) Glass-water interaction: Effect of high-valence cations on glass structure and chemical durability. Geochimica Et Cosmochimica Acta 181, 54-71.

Hopf, J. and Pierce, E. (2014) Topography and mechanical property mapping of International Simple Glass surfaces with atomic force microscopy. Procedia Materials Science 7, 216-222.

Icenhower, J.P., McGrail, B.P., Shaw, W.J., Pierce, E.M., Nachimuthu, P., Shuh, D.K., Rodriguez, E.A. and Steele, J.L. (2008) Experimentally determined dissolution kinetics of Na-rich borosilicate glass at far from equilibrium conditions: Implications for Transition State Theory. Geochimica Et Cosmochimica Acta 72, 2767-2788.

Icopini, G., Brantley, S. and Heaney, P. (2005) Kinetics of silica oligomerization and nanocolloid formation as a function of pH and ionic strength at 25°C. Geochimica et Cosmochimica Acta 69, 293-303.

Jollivet, P., Calas, G., Galoisy, L., Angeli, F., Bergeron, B., Gin, S., Ruffoni, M. and Trcera, N. (2013) An enhanced resolution of the structural environment of zirconium in borosilicate glasses. Journal of Non-Crystalline Solids 381, 40-47.

Jones, J. and Segnit, E. (1971) The nature of opal I. nomenclature and constituent phases. Australian Journal of Earth Sciences 18, 57-68.

ACCEPTED MANUSCRIPT

Langer, K. and Flörke, O. (1972) Near infrared absorption spectra (4000– 9000 cm-1) of opals and the role of ‘‘water’’ in the SiO2·nH2O minerals. Fortschritte der Mineralogie 52, 17-51.

Lenting, C., Dohmen, L. and Geisler, T. (2015) In situ, real-time, and isotope tracer glass corrosion experiments: understanding pattern formation in silicate glass corrosion zones, Glass Deterioration Colloquium - Extended Abstract, State Academy of Art and Design Stuttgart.

Lynne, B., Campbell, K., James, B., Browne, P. and Moore, J. (2007) Tracking crystallinity in siliceous hot-spring deposits. American Journal of Science 307, 612-641.

McGrail, B.P., Icenhower, J.P., Shuh, D.K., Liu, P., Darab, J.G., Baer, D.R., Thevuthasen, S., Shutthanandan, V., Engelhard, M.H., Booth, C.H. and Nachimuthu, P. (2001) The Structure of Na2O-Al2O3-SiO2 glass: Impact on Sodium Ion Exchange in H2O and D2O. Journal of Non-Crystalline Solids 296, 10-26.

McGrail, B.P., Lindenmeier, C.W. and Martin, P.F. (1998) Characterization of Pore Structure and Hydraulic Property Alteration in Pressurized Unsaturated Flow Tests, in: Wronkiewicz, D., Lee, J. (Eds.), Proceedings of the Materials Research Symposium: Scientific Basis for Nuclear Waste Management. Materials Research Society, Warrendale, PA, pp. 421-428.

McGrail, B.P., Lindenmeier, C.W., Martin, P.F. and Gee, G.W. (1996) The Pressurized Unsaturated Flow (PUF) Test: A New Method for Engineered-Barrier Material Evaluation, American Ceramic Society. American Ceramics Society, Indianapolis, Indiana.

McGrail, B.P., Martin, P.F., Lindenmeier, C.W. and Schaef, H.T. (1999) Application of the Pressurized Unsaturated Flow (PUF) Test for Accelerated Ageing of Waste Forms, Proceedings of the International Conference on Ageing Studies & Lifetime Extension of Materials, Oxford, UK.

McGrail, B.P., Pederson, L. and Petersen, D. (1986) The influence of surface potential and pH on the release of sodium from Na2O*3SiO2 glass. Physics and Chemistry of Glasses 27, 59-64.

McOrist, G. and Smallwood, A. (1997) Trace elements in precious and common opals using neutron activation analysis. Journal of Radioanalytical Nuclear Chemistry 223, 9-15.

McOrist, G., Smallwood, A. and Fardy, J. (1994) Trace elements in Australian opals using neutron activation analysis. Journal of Radioanalytical Nuclear Chemistry 185, 293-303.

Metrology, I. (2014) The Scanning Probe Image Processor: SPIP User's and Reference Guide., 6.3 ed, Denmark.

Muller, I.S., Buechele, A. and Pegg, I.L. (2001) Glass Formulation and Testing with RPP-WTP-LAW Simulants. Vitreous State Laboratory, The Catholic University of America, Washington, DC.

Murray, C., Flannery, C., Streiter, I., Schultz, S., Baklanov, M., Mogilnikov, K., Himcinschi, C., Friedrich, M., Zahn, D. and Gessner, T. (2002) Comparison of Techniques to Characterize the Density, Porosity, and Elastic Modulus of Porous low k-SiO2 xerogel films. Microelectronic Engieering 60, 133-141.

Neeway, J., Kerisit, S., Liu, J., Zhang, J., Zhu, Z., Riley, B. and Ryan, J. (2016) Ion-Exchange Interdiffusion Model with Potential Application to Long-Term Nuclear Waste Glass Performance. Journal of Physical Chemistry C 120, 9374-9384.

ACCEPTED MANUSCRIPT

Nicolau, C., Reich, M. and Lynne, B. (2014) Physico-chemical and environmental controls on siliceous sinter formation at the high-altitude El Tatio geothermal field, Chile. Journal of Volcanology and Geothermal Research 282, 60-76.

Nugent, M., Brantley, S., Pantano, C.G. and Maurice, P. (1998) The influence of natural mineral coatings on feldspar weathering. Nature 395, 588-591.

Pederson, L., Baer, D.R., McVay, G. and Engelhard, M.H. (1986) Reaction of soda lime silicate glass in isotopically labelled water. Journal of Non-Crystalline Solids 86, 369-380.

Pèlegrin, E., Calas, G., Ildefonse, P., Jollivet, P. and Galoisy, L. (2010) Structural evolution of glass surface during alteration: Application to nuclear waste glasses. Journal of Non-Crystalline Solids 356, 2497-2508.

Pierce, E. and Bacon, D. (2011) Combined Experimental and Computational Approach to Predict the Glass-Water Reaction. Nuclear Technology 176, 22–39.

Pierce, E., McGrail, B., Marra, J., Martin, P., Arey, B. and Geiszler, K. (2007) Accelerated Weathering of a High-Level and Pu-bearing Lanthanide Borosilicate Waste Glass in a Can-in-Canister Configuration. Applied Geochemistry 22, 1841−1859.

Pierce, E., McGrail, B., Rodriguez, E., Schaef, H., Saripalli, K., Serne, R., Krupka, K., Martin, P., Baum, S., Geiszler, K., Reed, L. and Shaw, W. (2004) Waste Form Release Data Package for the 2005 Integrated Disposal Facility Performance Assessment. Pacific Northwest National Laboratory, Richland, Washington.

Pierce, E., Reed, L., Shaw, W., McGrail, B., Icenhower, J., Windisch, C., Cordova, E. and Broady, J. (2010) Experimental Determination of the Effect of the Ratio of B/Al on Glass Dissolution Along the Nepheline (NaAlSiO4)–Malinkoite (NaBSiO4) Join. Geochimica et Cosmochimica Acta 74, 2634−2654.

Pierce, E., Richards, E., Davis, A., Reed, L. and Rodrigueza, E. (2008a) Aluminoborosilicate Waste Glass Dissolution under Alkaline Conditions at 40°C: Implications for a Chemical Affinity-based Rate Equation. Environmental Chemistry 5, 1–13.

Pierce, E., Rodriguez, E., Calligan, L., Shaw, W. and McGrail, B. (2008b) An Experimental Study of the Dissolution Rates of Simulated Aluminoborosilicate Waste Glasses as a Function of pH and Temperature under Dilute Conditions. Applied Geochemistry 23, 2559−2573.

Pierce, E.M., Frugier, P., Criscenti, L.J., Kwon, K.D. and Kerisit, S.N. (2014a) Modeling Interfacial Glass-water Reactions: Recent Advances and Current Limitations. International Journal of Applied Glass Science 5, 421-435.

Pierce, E.M., Lukens, W.W., Fitts, J.P., Jantzen, C.M. and Tang, G. (2014b) Experimental determination of the speciation, partitioning, and release of perrhenate as a chemical surrogate for pertechnetate from a sodalite-bearing multiphase ceramic waste form. Applied Geochemistry 42, 47-59.

Pierce, E.M., McGrail, B.P., Valenta, M.M. and Strachan, D.M. (2006) The accelerated weathering of a radioactive low-activity waste glass under hydraulically unsaturated conditions: Experimental results from a pressurized unsaturated flow test. Nuclear Technology 155, 149-165.

Putnis, A. (2015) Glass corrosion: Sharpened interface. Nature Materials 14, 261-262.

ACCEPTED MANUSCRIPT

Rajmohan, N., Frugier, P. and Gin, S. (2010) Composition effects on synthetic glass alteration mechanisms: Part 1. Experiments. Chemical Geology 279, 106-119.

Rimer, J., Lobo, R. and Vlachos, D. (2005) Physical Basis for the Formation and Stability of Silica Nanoparticles in Basic Solutions of Monovalent Cations. Langmuir 21, 8960-8971.

Rimer, J., Trofymulk, O., Lobo, R., Navrotsky, A. and Vlachos, D. (2008) Thermodynamics of silica nanoparticle self-assembly in basic solutions of monovalent cations. Journal of Physical Chemistry C 112, 14754-14761.

Rimer, J., Trofymulk, O., Navrotsky, A., Lobo, R. and Vlachos, D. (2007) Kinetic and Thermodynamic Studies of Silica Nanoparticle Dissolution. Chemistry of Materials 19, 4189-4197.

Rimza, J. and Du, J. (2014) Structural and Mechanical Properties of Nanoporous Silica. Journal of American Ceramic Society 97, 772-781.

Ruiz-Agudo, E., King, H., Patino-Lopez, L., Putnis, C., Geisler, T., Rodriguez-Navarro, C. and Putnis, A. (2016) Control of silicate weathering by interface-coupled dissolution-precipitation processes at the mineral-solution interface. Geology 44, G37856.37851.

Schalm, O. and Anaf, W. (2015) Laminated altered layers in historical glass: Density variations of silica nanoparticles random packings as explanation of the observed lamellae, Glass Deterioration Colloquium - Extended Abstracts, State Academy of Art and Design Stuttgart, pp. 53 - 59.

Schalm, O. and Anaf, W. (2016) Laminated altered layers in historical glass: Density variations of silica nanoparticle random packings as explanation for observed lamellae. Journal of Non-Crystalline Solids 442, 1-16.

Schneider, C., Rasband, W. and Eliceiri, K. (2012) NIH Image to ImageJ: 25 years of image analysis. Nature Methods 9, 671-675.

Smith, N., Rangarajan, B., Lanagan, M. and Pantano, C.G. (2009) Alkali-free glass as a high energy density dielectric material. Materials Letters 63, 1245-1248.

Stone-Weiss, N., Pierce, E., Youngman, R., Gulbiten, O., Smith, N., Du, J. and Goel, A. (2018) Understanding the structural drivers governing glass-water interactions in borosilicate based model bioactive glass. Acta Biomaterialia 65, 436-449.

Tobler, D., Shaw, S. and Benning, L. (2009) Quatification of initial steps of nucleation and growth of silica nanoparticles: An in-situ SAXS and DLS study. Geochimica et Cosmochimica Acta 73, 5377-5393.

Vienna, J.D., Ryan, J.V., Gin, S. and Inagaki, Y. (2013) Current Understanding and Remaining Challenges in Modeling Long-Term Degradation of Borosilicate Nuclear Waste Glasses. International Journal of Applied Glass Science 4, 283-294.

Wang, Y., Jove-Colon, C. and Kuhlman, K. (2016) Nonlinear dynamics and instability of aqueous dissolution of silicate glasses and minerals. Scientific Reports 6:30256, 1-8.

Williams, L. and Crerar, D. (1985) Silica Diagenesis II: General Mechanisms. Journal of Sedimentary Petrology 55, 312-321.

ACCEPTED MANUSCRIPT

Zachara, J., Brantley, S., Chorover, J., Ewing, R., Kerisit, S., Liu, C., Perfect, E., Rother, G. and Stack, A. (2016) Internal Domains of Natural Porous Media Revealed: Critical Locations for Transport, Storage, and Chemical Reaction. Environmental Science & Technology 50, 2811-2829.

Zarzycki, J. (1982) Glass Structure. Journal of Non-Crystalline Solids 52, 31-43.

ACCEPTED MANUSCRIPT

ACCEPTED MANUSCRIPT

8 FIGURES

Fig. 1. Normalized Concentration (a), in mg/L, as a function of time, in days, for Al, B, Ca, Fe, Li, Mg, Na, S, Si, Zn, and Zr. Normalized dissolution rate (b), in g/(m^2 d), as a function of time, in days, for Al, B, Ca, Fe, Li, Mg, Na, S, Si, Zn, and Zr. Measured concentrations for Fe, Mg, Zn, and Zr were all below detection limits and therefore represent maximum concentrations and maximum normalized release. 41

Fig. 2. High resolution TEM image of clay layer in a FIB lamella removed from reacted LAWB45 glass. Double diffraction can be observed in the FFT of the image. 42

Fig. 3. Time of flight secondary ion mass spectrometry elemental profile from a cross-sectioned reacted glass grain with a thick altered layer located on the LAWB45-1 sample. Positive ions (Al, B, Ca, Fe, H, Li, Mg, Na, Si, and Zr) and negative ions (C, OH) were analyzed following sputtering with Cs^+ beam. Scanning Electron Microscopy image of analysis location also provided. The total thickness of the altered layer analyzed in ToF-SIMS is 17.1 ±3.5 μm which corresponds to a 12.6 ±2.9 μm and 4.5 ±0.6 μm hydrated layer and clay layer, respectively. 43

Fig. 4. Scanning Transmission Electron Microscopy (STEM) and energy-dispersive spectroscopy images of a FIB section removed from a grain in the LAWB45-1 sample. The following denotes the different locations on the sample: G – glass, H – hydrated layer, and C – clay layer. The scale bar for all images is 5 μm. Individual STEM-EDS images are provided for Al, Ca, C, Fe, Mg, Na, O, Si, S, Zn, and Zr. 44

Fig. 5. Scanning Transmission Electron Microscopy (STEM) images of a FIB subsample from a grain in the cross-sectioned LAWB45-1 sample. The 9.2 μm long FIB subsample consists of 1.4 μm thick pristine glass layer (G), 5.5 μm thick hydrated layer (H), 2.4 μm thick clay layer (C), and a 0.6 μm thick epoxy layer. The 5.5 μm thick hydrated layer can be further subdivided into the following sub-layers: a 0.4 μm Na-depleted layer, a 2.3 μm porous hydrated layer, a 0.3 μm wide crack, and a 2.9 μm dense hydrated layer. Higher magnification images of the FIB subsample, on the bottom left (b) illustrate a series of transition zones between the porous and dense hydrated layer and on the bottom right (c) the transition between the denser hydrated layer and clay (c). Transition zones denoted by * in images. The line in image (a) represents the average intensity of the dark-field image and suggests the amount of material remains constant throughout the altered layer. 45

Fig. 6. Quantitative Nanomechanical Peak Force® (PF-QNM) scan (512 × 512 pixel map) of the cross-sectioned LAWB45-1 sample. A stiffness histogram and 2D images of height (a), peak force error (b), modulus (c), log modulus (d), adhesion (e), and deformation (f) are also provided. 46

Fig. 7. A combination of bright-field Transmission Electron Microscopy (BF-TEM), scanning electron secondary electron (SE SEM), and bright- and dark-field scanning TEM (BF STEM and DF STEM) images of a FIB lamella removed from a grain in the LAWB45-1 sample. 47

Fig. 8. Dark field STEM image of the cross-sectional FIB lamella (a) showing the different layers from left to right: epoxy, clay, hydrated layer, bulk glass. Zoomed in region of the hydrated layer showing the porous nature of the hydrated layer with a qualitative estimate of porosity of ≥ 22% (b). Labels include glass (G), hydrated layer (H), and clay layer (C). 48

Fig. 9. STEM EELS-SI elemental signal maps of a thin corner of the hydrated glass layer. The Al-K, Si-K, and Zr-L regions were fit with a Hartee-Slater cross-section model and extracted. The combination maps show the localized element nature of the hydrated glass layer. Element colors are as follows: Green = Aluminum, Blue = Silicon, and Red = Zirconium. 49

Fig. 10. Selected-area electron diffraction (SAED) image of opal-A (a) and the hydrated layer (b). 2θ plot comparison (c) of the literature (Eckert et al., 2015) powder XRD patter for opal-A and the extracted radial intensity from the SAED image converted into 2θ using Braggs law and the Cu-Kα wavelength of 1.5418 Å. 50

ACCEPTED MANUSCRIPT

Fig. 11. Fourier-ratio deconvoluted electron energy loss spectrum intensity maps and average line profiles of the Si-L shell and B-K shell regions at the glass/hydrated layer interface. On the left side of each image is the bulk glass layer while on the right side is the hydrated layer. Average background extracted electron energy loss spectra of the Si-L shell and B-K shell energy regions extracted from the bulk glass, interface, and hydrated layers, respectively. 51

ACCEPTED MANUSCRIPT

ACCEPTED MANUSCRIPT

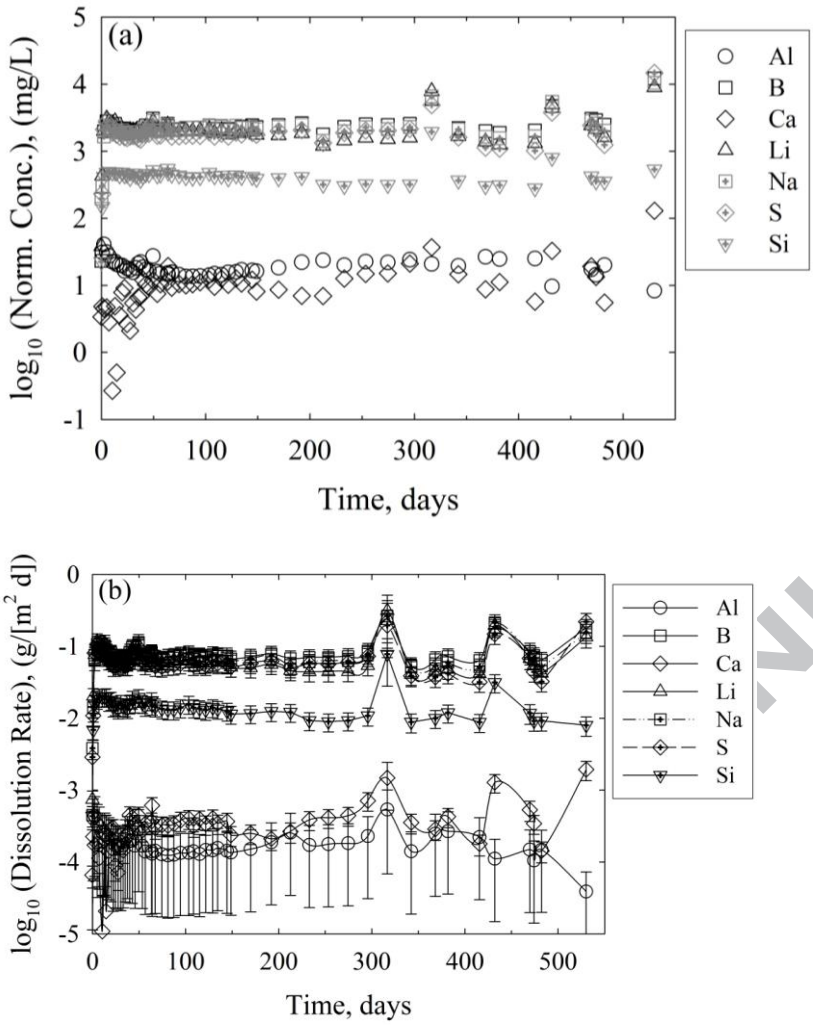

Fig. 1. Normalized Concentration (a), in mg/L, as a function of time, in days, for Al, B, Ca, Fe, Li, Mg, Na, S, Si, Zn, and Zr. Normalized dissolution rate (b), in g/(m^2 d), as a function of time, in days, for Al, B, Ca, Fe, Li, Mg, Na, S, Si, Zn, and Zr. Measured concentrations for Fe, Mg, Zn, and Zr were all below detection limits and therefore represent maximum concentrations and maximum normalized release.

ACCEPTED MANUSCRIPT

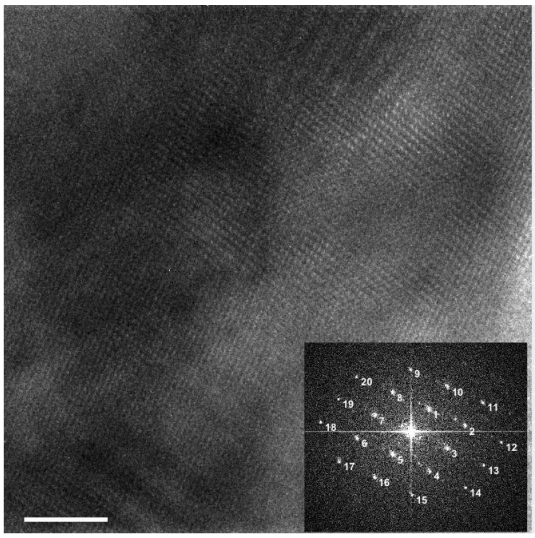

Spot#	Miller Index	d-Spacing (nm)	Lit. D-spacing
1	-110	0.459	0.451
2	-13-2	0.243	0.222
3	02-2	0.330	0.331
4	11-2	0.303	0.360
5	1-10	0.456	0.451
6	1-32	0.243	0.222
7	0-22	0.332	0.331
8	-1-12	0.306	0.360
9	-202	0.211	0.212
10	-220	0.228	0.225
11	-24-2	0.170	0.155
12	-15-4	0.145	0.144
13	04-4	0.166	0.165
14	13-4	0.170	0.186
15	20-2	0.210	0.212
16	2-20	0.227	0.225
17	2-42	0.171	0.155
18	1-54	0.146	0.144

Fig. 2. High resolution TEM image of clay layer in a FIB lamella removed from reacted LAWB45 glass. Double diffraction can be observed in the FFT of the image.

ACCEPTED MANUSCRIPT

ACCEPTED MANUSCRIPT

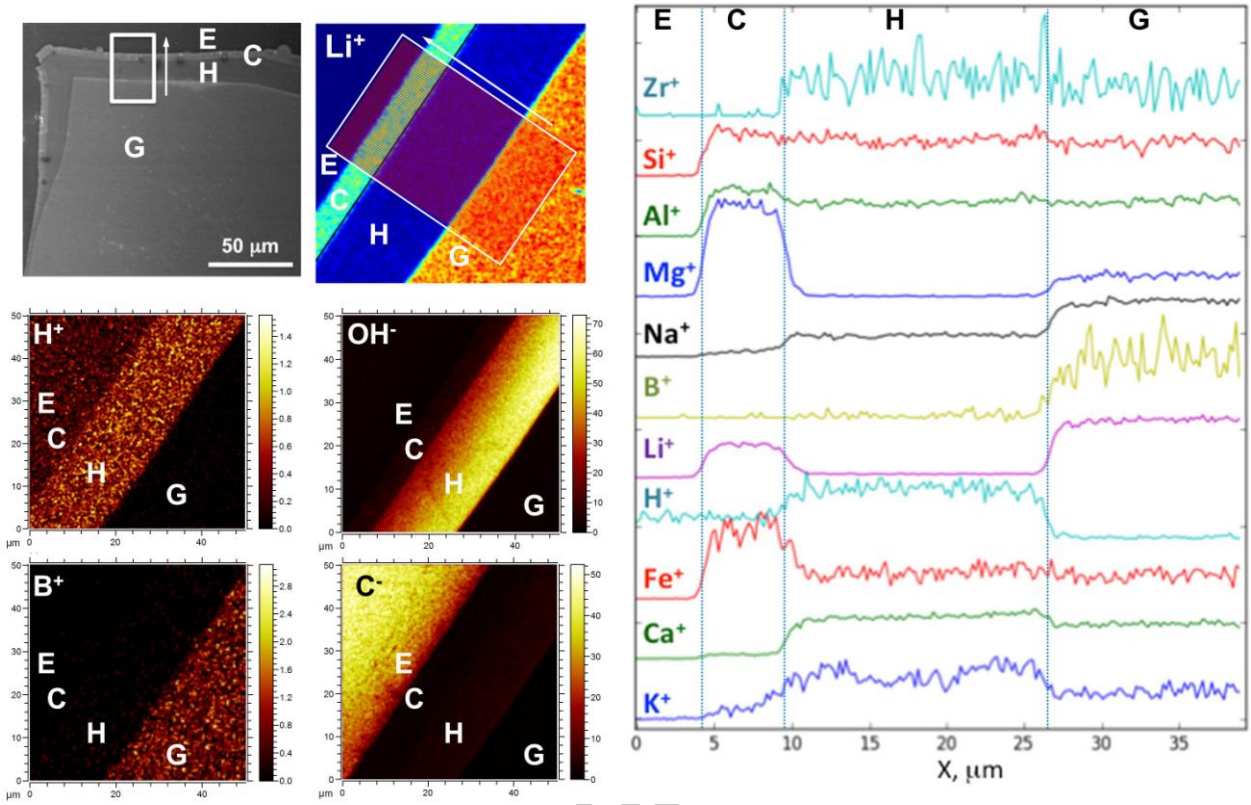

Fig. 3.. Time of flight secondary ion mass spectrometry elemental profile from a cross-sectioned reacted glass grain with a thick altered layer located on the LAWB45-1 sample. Positive ions (Al, B, Ca, Fe, H, Li, Mg, Na, Si, and Zr) and negative ions (C, OH) were analyzed following sputtering with Cs^+ beam. Scanning Electron Microscopy image of analysis location also provided. The total thickness of the altered layer analyzed in ToF-SIMS is 17.1 ±3.5 µm which corresponds to a 12.6 ±2.9 µm and 4.5 ±0.6 µm hydrated layer and clay layer, respectively.

ACCEPTED MANUSCRIPT

ACCEPTED MANUSCRIPT

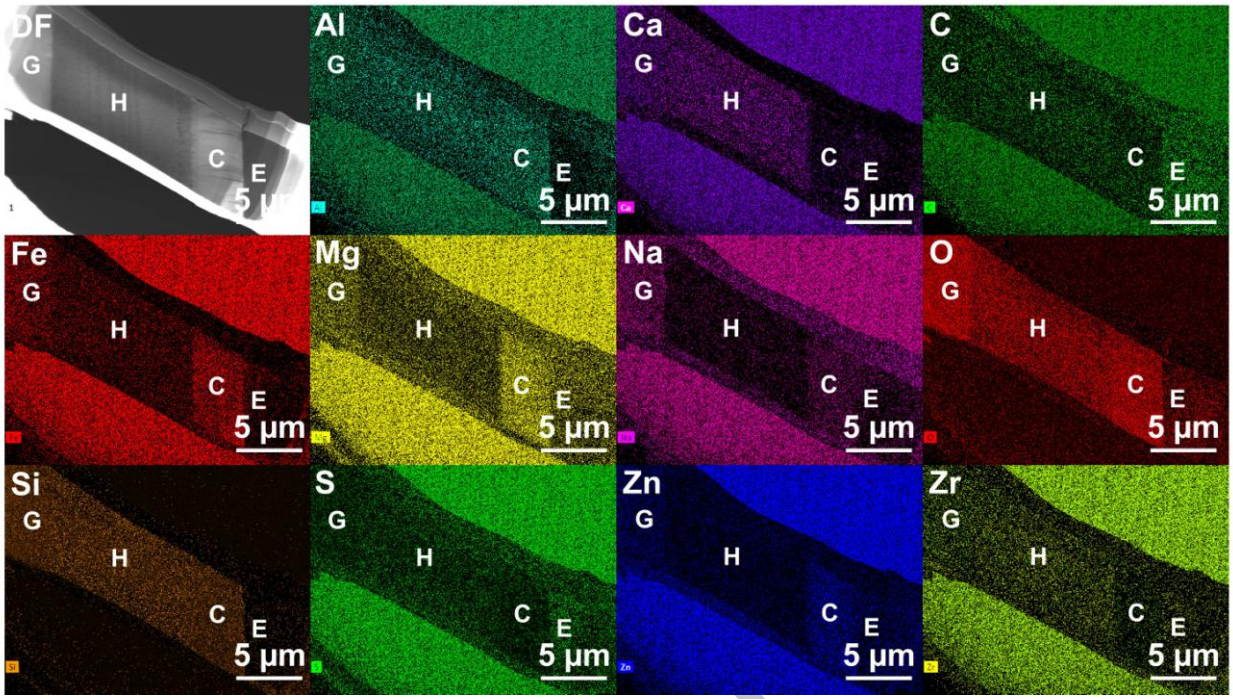

Fig. 4. Scanning Transmission Electron Microscopy (STEM) and energy-dispersive spectroscopy images of a FIB section removed from a grain in the LAWB45-1 sample. The following denotes the different locations on the sample: G – glass, H – hydrated layer, and C – clay layer. The scale bar for all images is 5 µm. Individual STEM-EDS images are provided for Al, Ca, C, Fe, Mg, Na, O, Si, S, Zn, and Zr.

ACCEPTED MANUSCRIPT

ACCEPTED MANUSCRIPT

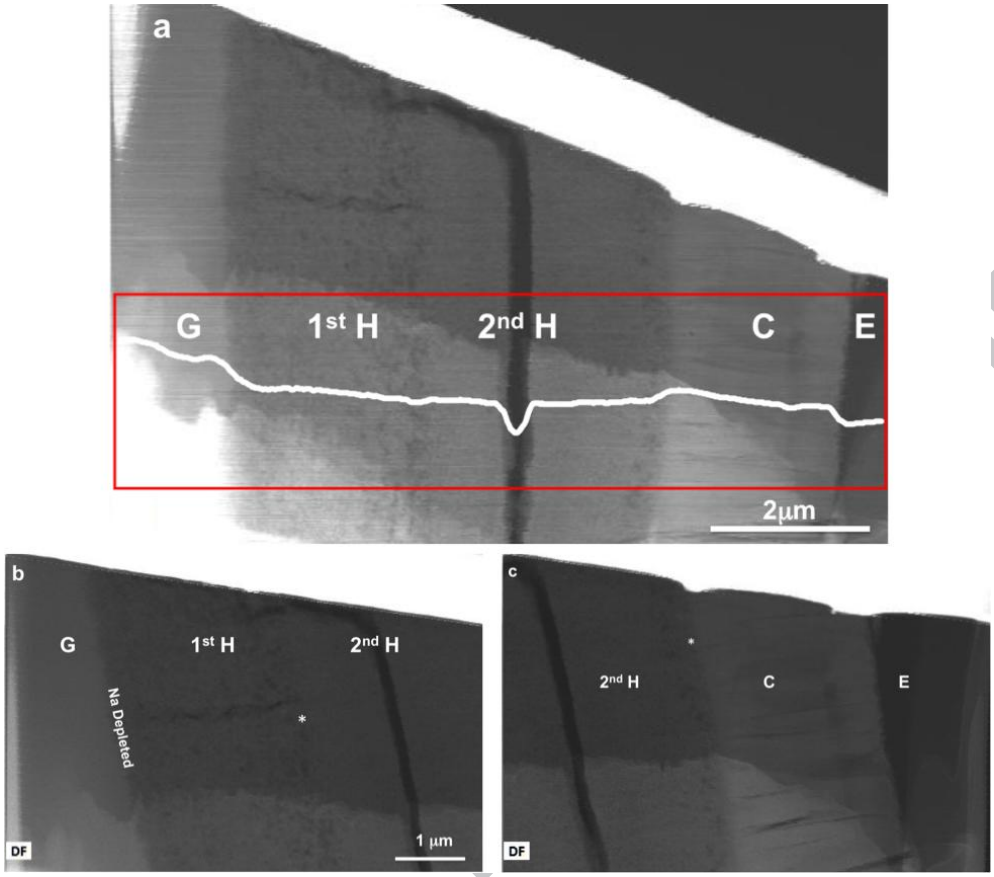

Fig. 5. Scanning Transmission Electron Microscopy (STEM) images of a FIB subsample from a grain in the cross-sectioned LAWB45-1 sample. The 9.2 μm long FIB subsample consists of 1.4 μm thick pristine glass layer (G), 5.5 μm thick hydrated layer (H), 2.4 μm thick clay layer (C), and a 0.6 μm thick epoxy layer. The 5.5 μm thick hydrated layer can be further subdivided into the following sub-layers: a 0.4 μm Na-depleted layer, a 2.3 μm porous hydrated layer, a 0.3 μm wide crack, and a 2.9 μm dense hydrated layer. Higher magnification images of the FIB subsample, on the bottom left (b) illustrate a series of transition zones between the porous and dense hydrated layer and on the bottom right (c) the transition between the denser hydrated layer and clay (c). Transition zones denoted by * in images. The line in image (a) represents the average intensity of the dark-field image and suggests the amount of material remains constant throughout the altered layer.

ACCEPTED MANUSCRIPT

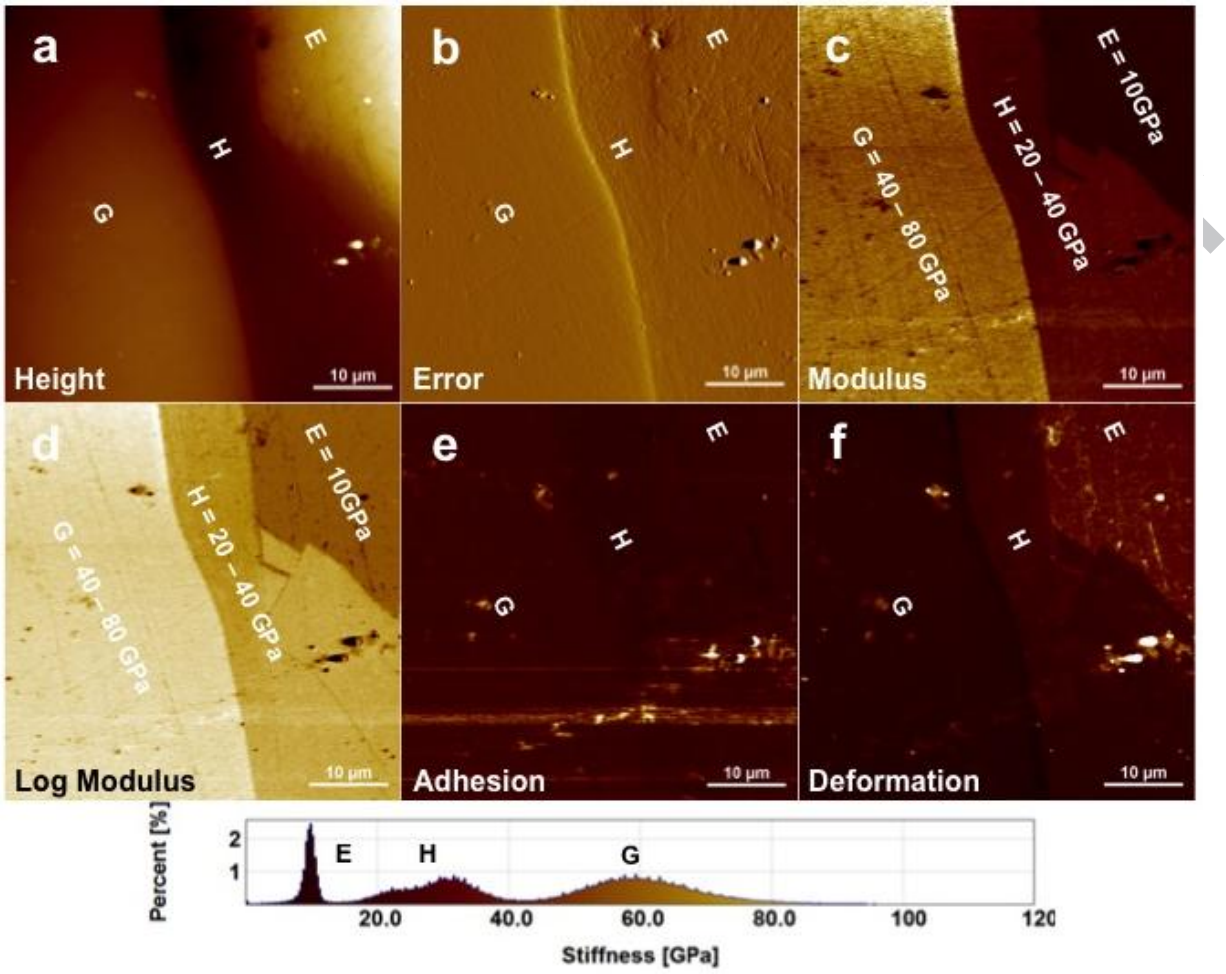

Fig. 6. Quantitative Nanomechanical Peak Force® (PF-QNM) scan (512 × 512 pixel map) of the cross-sectioned LAWB45-1 sample. A stiffness histogram and 2D images of height (a), peak force error (b), modulus (c), log modulus (d), adhesion (e), and deformation (f) are also provided.

ACCEPTED

ACCEPTED MANUSCRIPT

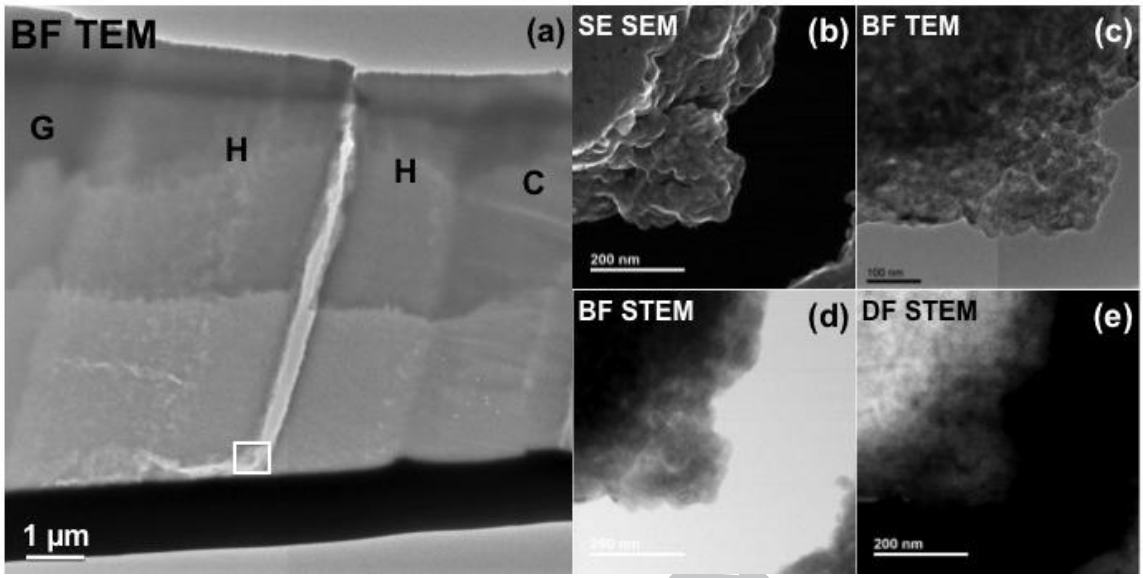

Fig. 7. A combination of bright-field Transmission Electron Microscopy (BF-TEM), scanning electron secondary electron (SE SEM), and bright- and dark-field scanning TEM (BF STEM and DF STEM) images of a FIB lamella removed from a grain in the LAWB45-1 sample.

ACCEPTED MANUSCRIPT

ACCEPTED MANUSCRIPT

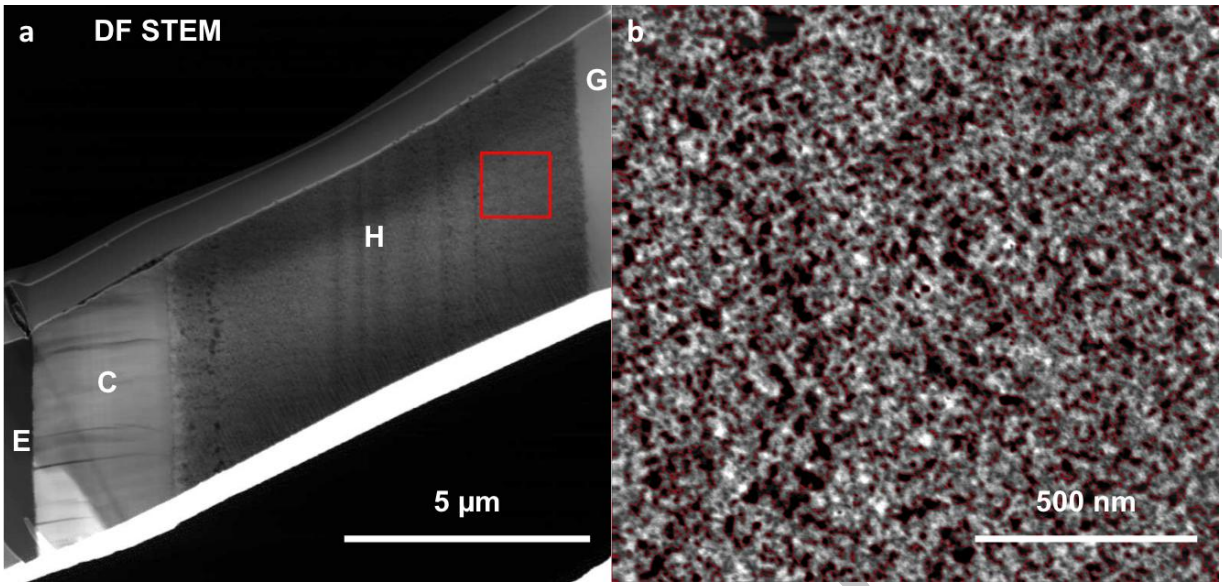

Fig. 8. Dark field STEM image of the cross-sectional FIB lamella (a) showing the different layers from left to right: epoxy, clay, hydrated layer, bulk glass. Zoomed in region of the hydrated layer showing the porous nature of the hydrated layer with a qualitative estimate of porosity of ≥ 22% (b). Labels include glass (G), hydrated layer (H), and clay layer (C).

ACCEPTED MANUSCRIPT

ACCEPTED MANUSCRIPT

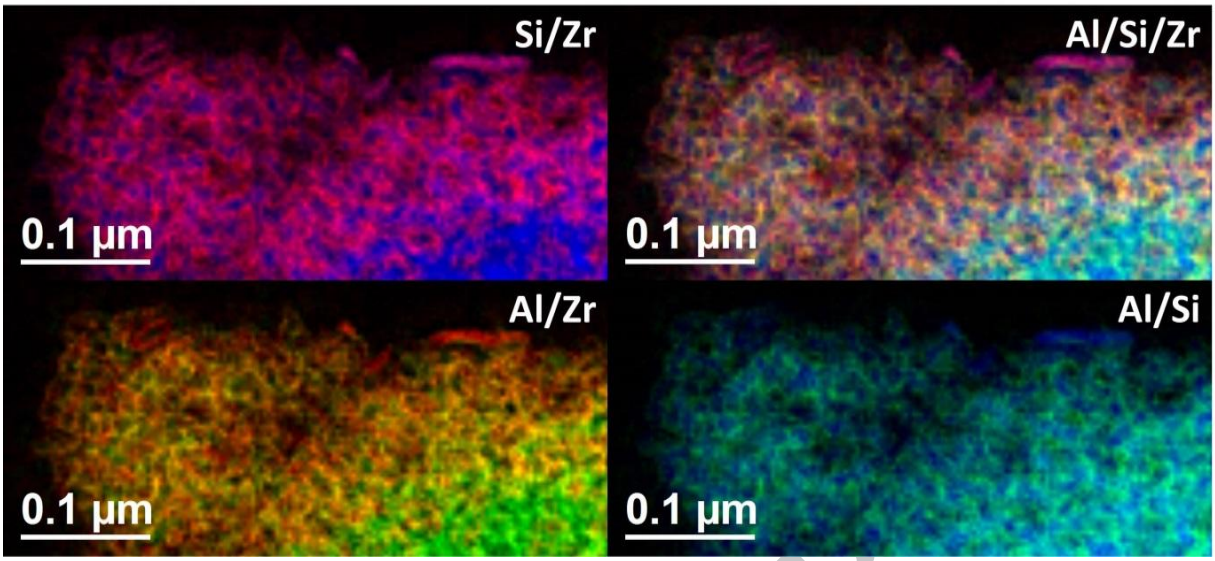

Fig. 9. STEM EELS-SI elemental signal maps of a thin corner of the hydrated glass layer. The Al-K, Si-K, and Zr-L regions were fit with a Hartee-Slater cross-section model and extracted. The combination maps show the localized element nature of the hydrated glass layer. Element colors are as follows: Green = Aluminum, Blue = Silicon, and Red = Zirconium.

ACCEPTED MANUSCRIPT

ACCEPTED MANUSCRIPT

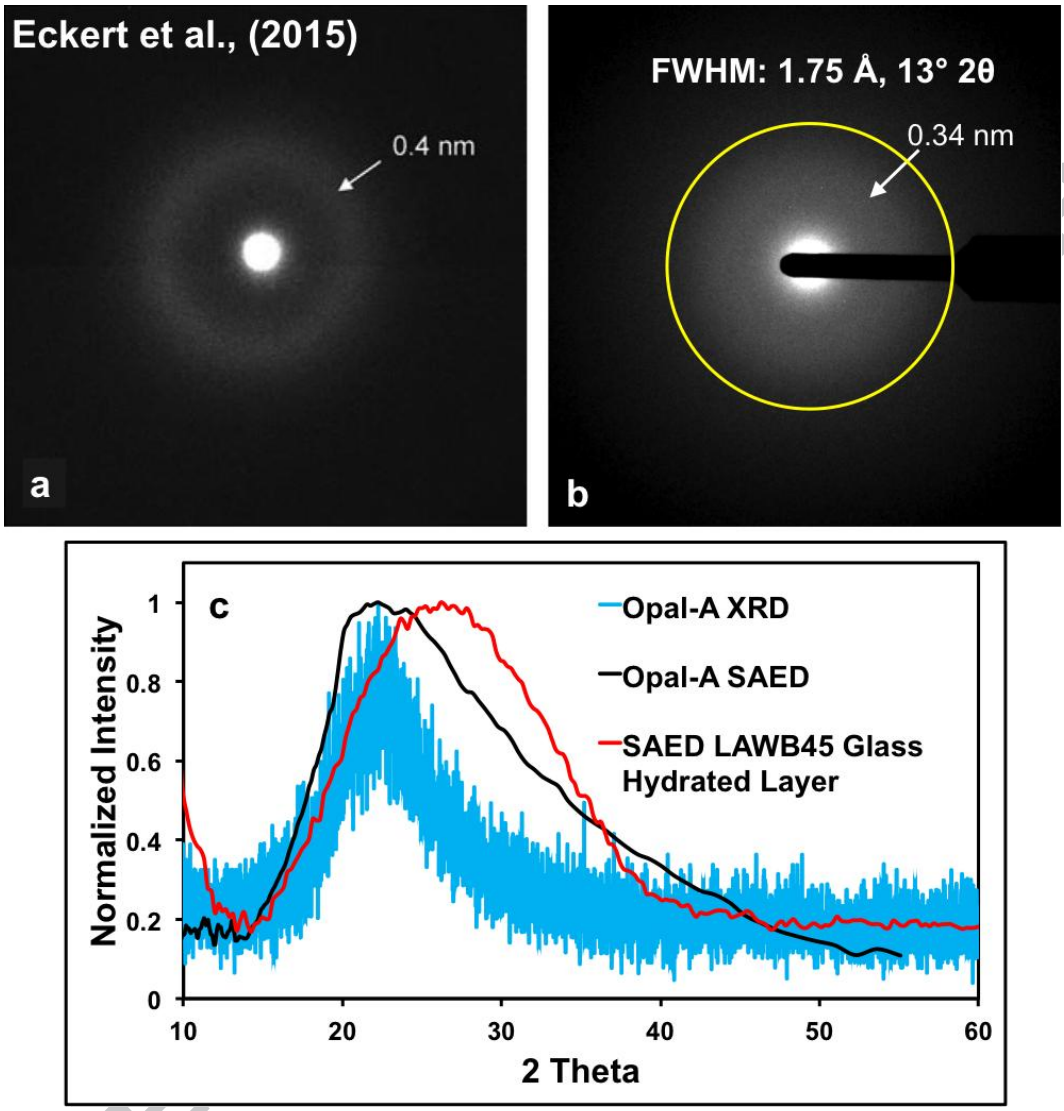

Fig. 10. Selected-area electron diffraction (SAED) image of opal-A (a) and the hydrated layer (b). 2θ plot comparison (c) of the literature (Eckert et al., 2015) powder XRD patter for opal-A and the extracted radial intensity from the SAED image converted into 2θ using Braggs law and the Cu-Kα wavelength of 1.5418 Å.

ACCEPTED MANUSCRIPT

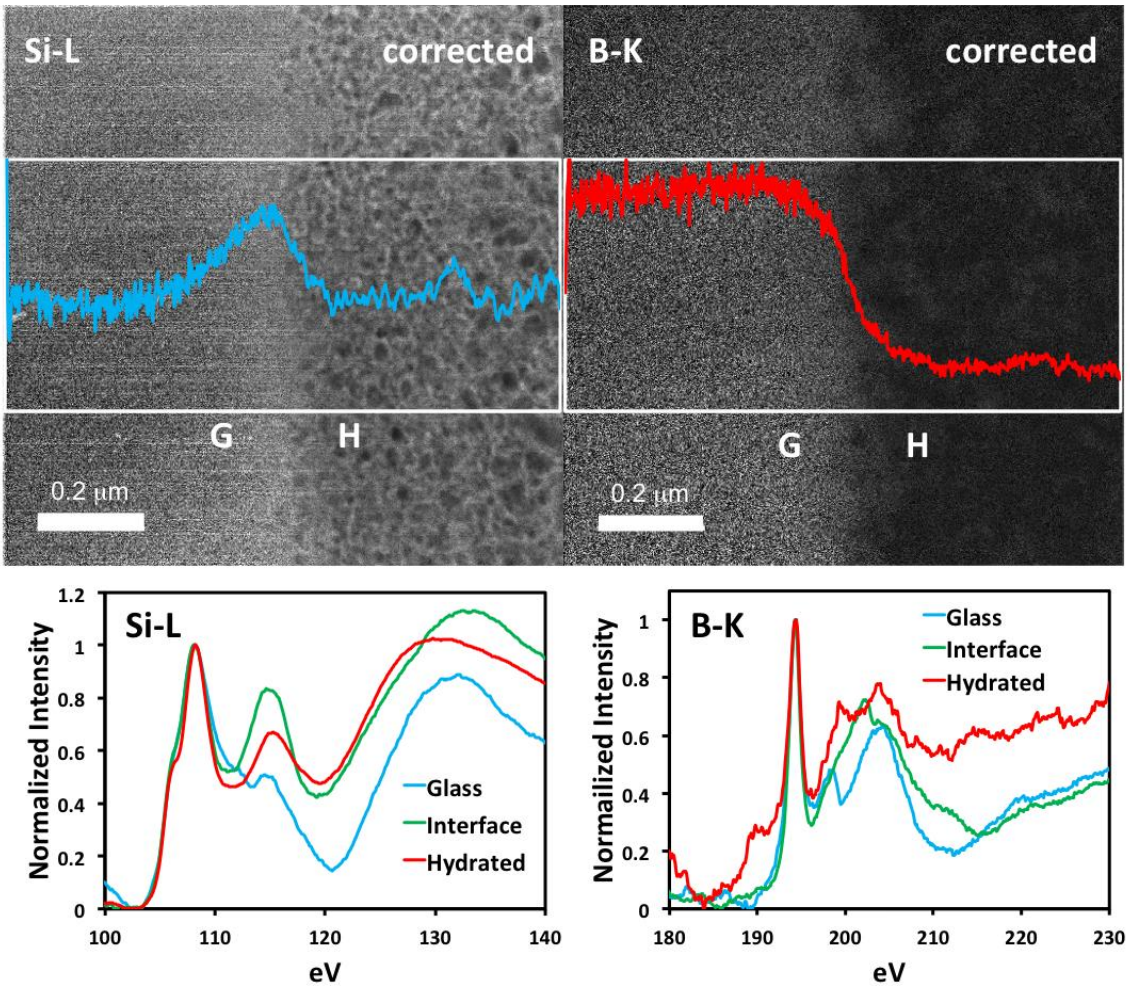

Fig. 11. Fourier-ratio deconvoluted electron energy loss spectrum intensity maps and average line profiles of the Si-L shell and B-K shell regions at the glass/hydrated layer interface. On the left side of each image is the bulk glass layer while on the right side is the hydrated layer. Average background extracted electron energy loss spectra of the Si-L shell and B-K shell energy regions extracted from the bulk glass, interface, and hydrated layers, respectively.

ACCEPTED MANUSCRIPT

Tables

Table 1. Average, standard deviation, minimum, maximum thickness measurements for the altered layer, hydrated layer, and clay layer for LAWB45-1 sample. Results are based on the analysis of 40 images with average of 94 to 166 measurements per image for the hydrated and clay layers, respectively. 52

Table 2. Estimates of tau (τ) values for Al, Ca, Fe, Mg, Na, O, Si, and Zn based on STEM-EDS measurements for different region on a FIB sample of LAWB45-1. Zr represents the immobile element. 52

Table 3. Full-Width Half Maximum comparison between LAWB45 hydrated layer and opal-A, opal-A/CT, opal-CT, opal-C, and quartz. Also provided is a crystallite size comparison using the Scherrer Equation. 53

Table 1. Average, standard deviation, minimum, maximum thickness measurements for the altered layer, hydrated layer, and clay layer for LAWB45-1 sample. Results are based on the analysis of 40 images with average of 94 to 166 measurements per image for the hydrated and clay layers, respectively.

	Hydrated Layer (μm)	Clay Layer (μm)	Altered Layer Thickness Total (μm)
Average	9.9 ±6.2	3.3 ±2.1	13.2 ±8.3
Min	0.01	0.36	0.37
Max	42.8	25.2	68.0

Table 2. Estimates of tau (τ) values for Al, Ca, Fe, Mg, Na, O, Si, and Zn based on STEM-EDS measurements for different region on a FIB sample of LAWB45-1. Zr represents the immobile element.

	τ-Zr	τ-Al	τ-Ca	τ-Fe	τ-Mg	τ-Na	τ-O	τ-Si	τ-Zn
bulk glass	0	0	0	0	0	0	0	0	0
Na depleted	0	0.23	-0.11	-0.29	-0.39	-0.45	-0.15	-0.09	-0.36
1st porous	0	0.17	-0.32	-0.63	-0.80	-0.80	-0.51	-0.46	-0.76
2nd porous	0	0.29	-0.47	-0.62	-0.71	-0.84	-0.61	-0.58	-0.71

ACCEPTED MANUSCRIPT

Table 3. Full-Width Half Maximum comparison between LAWB45 hydrated layer and opal-A, opal-A/CT, opal-CT, opal-C, and quartz. Also provided is a crystallite size comparison using the Scherrer Equation.

Sample	FWHM (°2θ)	Crystallite Size (Å)	Reference
Hydrated Layer	13	7.0	This Study
Opal-A	12.5 – 6.1		(Lynne et al., 2007; Nicolau et al., 2014)
Opal-A/CT	6.0 – 2.7		(Lynne et al., 2007)
Opal-CT	2.5 – 1.0		(Lynne et al., 2007)
Opal-C	0.9 – 0.4		(Lynne et al., 2007)
Quartz	0.4 – 0.1		(Lynne et al., 2007)

ACCEPTED MANUSCRIPT